ASTRONOMY & ASTROPHYSICS
SUPPLEMENT SERIES

Astron. Astrophys. Suppl. Ser. **114,** 51-78 (1995)

CCD imaging of ultra-steep-spectrum radio sources

H.J.A. Röttgering[1,2,3], G.K. Miley[1], K.C. Chambers[4] and F. Macchetto[5,6]

[1] Leiden Observatory, P.O. Box 9513, 2300 RA, Leiden, The Netherlands
[2] Mullard Radio Astronomy Observatory, Cavendish Laboratory, Madingley Road, Cambridge, CB3 0HE, UK
[3] Institute of Astronomy, Madingley Road, Cambridge, CB3 0HA, UK
[4] Institute for Astronomy, University of Hawaii, 2680 Woodlawn Drive, Honolulu, HI 96822, U.S.A.
[5] Space Telescope Science Institute, Baltimore
[6] Affiliated with Space Science Department of ESA

Received October 20, 1994; accepted May 22, 1995

Abstract. — We present deep R band CCD images of a sample of 88 radio sources. The sources have an ultra-steep radio spectra and are taken from the Texas, Parkes and Molonglo catalogues. Of the 80 sources that do not have a diffuse radio morphology, 53 sources are identified to a limiting magnitude of $R \sim 24$. The reliability and completeness of the identifications are discussed using a likelihood method which takes into account the sizes of the radio sources. Basic source parameters, such as optical magnitudes, position angles and ellipticities are derived from the images. The distribution of the R-magnitudes peaks at $22.5 < R < 23$, and is consistent with all the radio sources being associated with objects brighter than $R = 24$.

Key words: astronomical data bases: surveys — galaxies: active — radio continuum: galaxies

1. Introduction

Radio sources with an ultra-steep spectrum (USS, $S \sim \nu^{\alpha}$, $\alpha \lesssim -1.0$) are a powerful tool for pinpointing distant galaxies (e.g. Miley & Chambers 1989; Chambers & Miley 1989). We have started a project to exploit this technique, thereby increasing the number galaxies $z > 2$ for further studies. The main steps of the project are i) selection of samples of sources with an ultra-steep spectra, ii) high-resolution radio imaging with the VLA, iii) R band CCD imaging, iv) optical spectroscopy to determine redshifts and v) detailed studies of the discovered high-redshift galaxies. An account of the background and the main aims of this programme can be found in Röttgering (1993). The definition of the samples of USS sources and the results of high resolution (1.5″) imaging of sources from these samples with the VLA at 1465 MHz is described in Röttgering et al. (1994). Here we presents the first results of R band CCD imaging of these samples using the ESO-MPI 2.2 m telescope.

The primary aim of the CCD imaging was to find optical counterparts for the USS radio sources. Not only was the imaging an important preliminary for carrying out spectroscopy, but the resulting database of CCD images can be used to carry out a study of morphologies of the optical counterparts of USS sources and the environment around them. Such studies will be described in subsequent papers.

The structure of this paper is as follows. First, we describe the observations and reduction of the imaging data. Second, we shall discuss the reliability and completeness of our identifications using a likelihood method. Third, the morphological parameters for the optical counterparts will be presented.

2. Selection of targets

Since the declination range accessible from La Silla (ESO) is $\delta \lesssim 20°$, we restricted our observation to sources from the Parkes, Texas & Molonglo selected samples of the Röttgering et al. (1994) compendium. Selecting steep-spectrum sources ($\alpha < -0.5$) smaller than 60″ from the complete 3C sample (Laing et al. 1983) selects 70% of the $z > 0.1$ galaxies and 100% of the $z > 1.5$ quasars while rejecting 95% of the nearby $z < 0.1$ sources. Therefore, we preferentially observed the smaller ($< 20''$) sources to optimise our chances of finding distant galaxies.

3. Observations

The observations described here were made during four observing sessions, all with the ESO-MPI 2.2 m telescope. For details on dates and instrumentation see Table 1 and

Send offprint requests to: H.J.A. Röttgering: Leiden Observatory, P.O. Box 9513, 2300 RA, Leiden, The Netherlands

Table 1. Log of Observations with ESO-MPI 2.2 m Telescope

Observing Session	Dates	CCD	CCD Size	Binning	Median seeing (FWHM)
1	23 – 27 Aug 1989	RCA #11	1024 × 640	2 × 2	1.3″
2	1 – 6 March 1990	RCA #11	,,	2 × 2	1.0″
3	24 – 27 Oct 1990	RCA #5	512 × 320	–	1.2″
4	16 – 18 March 1991	RCA #5	,,	–	1.5″

the ESO Users Manual (Schwarz & Melnick 1989). A list of the targets observed is given in Appendix A.

All the objects were observed in the R band ($\lambda_{\rm eff} \sim$ 6900 Å; $\Delta\lambda_{\rm eff} \sim 1000$ Å). At the R band, the RCA chip has a serious fringing problem due to thin film interference. To assist in the fringe removal and to improve flat-fielding the 45-min total exposures were divided into three separate exposures of 900-s, each offset from each other by $10'' - 15''$. Each 900 s observation was sky limited. The seeing varied from $0.8''$ to $> 2.0''$ FWHM; the value for each source is listed in Appendix A.

Flux calibration was carried out using flux standards from the "E–regions" (Graham 1982). Typically three standard fields were observed, one at the beginning, one in the middle and one at the end of the night.

4. Reduction

The reduction was carried out with the standard software packages AIPS from NRAO and IRAF from NOAO.

Initially an averaged bias frame was subtracted from all the frames. The next step consisted in determining the optimum flat field by which object frames would be divided to correct for the pixel to pixel variations in quantum efficiencies and to minimise the effects of fringing.

We experimented with using i) an average of $\gtrsim 10$ dome flats taken by uniformly illuminating a screen on the dome using an external lamp or faint daylight, ii) short sky frames taken during twilight and dawn and iii) night-sky frames constructed using a combination of the target frames themselves. The latter resulted in the most uniform background and was used throughout. The procedure for constructing this internal flat field was to normalise each "object" frame to the median of the background of all the intensities in the field and then combine all the object frames, taking the median intensities at each pixel. This procedure removes the effects of stars and galaxies, whose positions differ from frame to frame.

Because the fringing was not constant from night to night (and sometimes varied even within a night) the construction of these internal flat fields had to be carried out seperately for each night, and sometimes even for parts of nights.

After the target frames had been flat-fielded, the three exposures of each object were registered in position using a dozen stars in the field and then summed. A first-order cosmic ray removal was performed using an algorithm that finds the cosmic ray events by comparing the value of an individual pixel with the mean of the surrounding pixels in a 7×7 pixel box and subsequently removing the cosmics. Typically $500-600$ cosmic ray events were removed. Faint cosmic ray events and cosmic ray events that hit the CCD at a large angle are difficult to discriminate from sky noise and could not always be removed.

Astrometric calibration of the CCD positions was carried out using the Guide Star Catalogue (GSC) image processing system of the Space Telescope Science Institute (Lasker et al. 1990). This system has an intrinsic accuracy of $\sim 0.7''$. Typically, $3-7$ stars or faint galaxies were visible on the CCD frames and on the GSC plate material. When more than 4 stars or faint galaxies were common, we solved for the scale, rotation, and positional zero point of the CCD frame. The pixel scale was found to be extremely stable for the four observing sessions and was determined to be $0.351'' \pm 0.001''$ per pixel. In about a quarter of the cases less than 4 common stars were available for a position solution and a single star was taken as the position reference. The astrometric position of an object was found from this reference position using the mean CCD rotation and pixel separation scale. The remaining stars were used to check the consistency of the positions. The resulting optical position uncertainty is a function of the number of reference stars and their position with respect to the optical identification. Adding this uncertainty estimated to be $\sim 0.3''$ and the GSC uncertainty in quadrature we estimate the final position error to be typically $0.9''$.

Finally the images were flux-calibrated using the measured standard stars. The agreement between the relevant conversion factors has been used to estimate the photometric accuracy of the observatation. The agreement between the photometric zero point determined from the three standard stars was on the photometric nights $\lesssim 0.1$ mag. For the other nights the agreement was better than about 0.5 mag.

5. Reduced images

The list of the 99 targets that we have observed is presented in Appendix A. Of the radio sources that were observed 10 were so close to a bright star or to a diffraction spike of a bright star that identifying the radio source was either impossible or seriously hampered. These objects are indicated by the codes 'b' (bright star) and 's' spike of bright star. The data of another source (0927+064) was contaminated due to a pointing problem. These 11 sources were rejected for further study. The total number of remaining sources is 88. In Table 2 we give a summary of the total number of radio sources and the name of the samples from which they come as designated in Röttgering et al. (1994). Note that 5 sources belong to more than one sample (see Appendix A).

Table 2. Number of sources imaged

Sample	178	365A	365B	408A	408B
No.	19	30	39	12	4

6. Detection

The identification of objects on the CCD frames with the USS radio galaxies was carried out in two steps. First, all objects detected in the frame were catalogued and their object parameters were determined. Second, identification with the radio source was made on the basis of i) the radio/optical position differences, ii) the background counts and iii) the radio source sizes.

The detection of faint objects on the CCD exposures is complicated, for at least three reasons. First, since the fringe pattern of the CCD chips that we used is time variable, its effects could not be removed perfectly. Second, as we remarked above, because cosmic ray events are not always bright single pixel effects, they cannot all be removed perfectly. Third, occasionally diffraction spikes and scattered light from bright stars on or near the CCD frame affected large regions of the frames, confusing the detections.

To detect and classify the objects on our CCD frames we used the Faint Object and Classification System (FOCAS, Valdes 1982). The intensity of a particular pixel was considered to be significantly different from the sky if the average background-subtracted intensity of this pixel and those from eight contiguous pixels was 2.5 times higher than the rms of the sky background. Intensity islands on the CCD that contain more than 25 contiguous significant pixels (1 pixel = $0.351'' \times 0.351''$) were considered to be possibly part of an object. A point spread function (PSF) was constructed for most frames using stars in the field. Candidate objects were fitted by the PSF and classified as noise if they were smaller than 0.6×PSF, as stars if their sizes were $0.61 - 1.20\times$ PSF and as galaxies $1.21 - 10.00\times$PSF. If the size of the object was $> 10.00\times$ PSF, the candidate object was attributed to flat fielding problems, effects of diffraction spikes, or cosmetic defects in the chip and rejected as a real object.

To derive object counts from our CCD frames we defined a subset of good images from the total sample of 88 CCD frames. CCD frames were rejected from the sample on the basis of the presence in the field of i) one or more bright stars or galaxies, ii) some residual fringing, iii) diffraction spikes from stars outside the field of view of the CCD or iv) large-scale gradients in the background. Since our goal was to identify distant radio galaxies, we included only the powerful radio sources that had a galaxy and not a QSO as possible identification. This resulted in a subset of 30 CCD frames.

For this subset of 30 frames we plot the density of objects as a function of R-magnitude in Fig. 1. The errors bars in Fig. 1 are merely the square root of the number of objects in the bin.

Deep R band CCD surveys indicate that the number counts can be well represented by a powerlaw down to at least $R \sim 26$ (Tyson 1988). The number counts for our data starts to deviate from a powerlaw at about $R \sim 23$, indicating that the counts are complete to $R \sim 23$. For $R \gtrsim 23$ the diagram indicates that we start missing objects. The local maximum in the counts between $R = 20$ and $R = 20.5$ is probably due to stars in our galaxy (Bahcall & Soneira 1984; Hill & Lilly 1991).

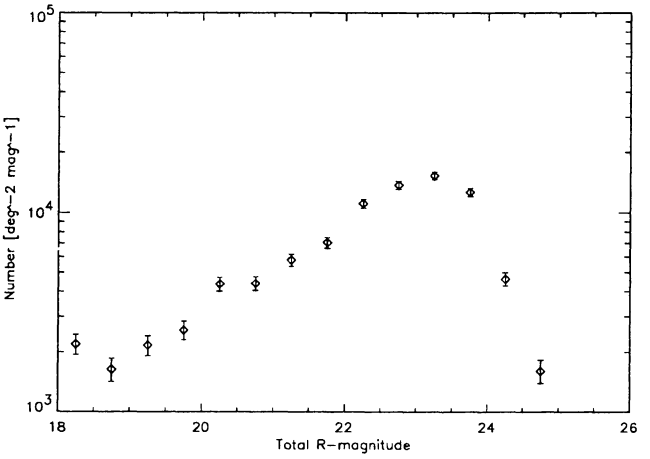

Fig. 1. Object counts as a function of R- magnitude

To judge the validity of a given identification it is important to estimate the mean density of objects to our limiting magnitude. Integrating our number counts (e.g. Fig. 1) we find that the mean density of objects on our CCD frames is $6\ 10^4$ deg^{-1} down to $R = 24.75$.

6.1. *Criteria for identification*

Identifying a radio source with the optical image of a galaxy is not a trivial task. Simple positional coincidence is an insufficient criterion. Both the radio sources and the galaxies are spatially extended and the radio and optical sizes are usually hugely different. It is therefore important to devise an objective procedure for identification to enable the statistical properties of the identified objects to be analysed.

We make use of the fact that, in previously studied distant radio sources the optical objects tend to lie along the radio structure, which is usually highly elongated and often linear. Most luminous radio sources are double lobed with well-defined extremities. The position of the optical counterpart with respect to these extremities can be studied using the "arm-length ratio" Q, defined as the ratio of the distance between the optical counterpart and the more distant radio extremity to the distance between the optical counterpart and the closer radio extremity.

The most complete data that are available for such statistical studies are those which characterise the 3CR (Bennett 1962) or the more restricted (but better defined) 3CRR (Laing et al. 1983). The distribution of this parameter Q for the sample of double lobed 3CR galaxies has been studied by McCarthy et al. (1991). This distribution is peaked at unity, has a mean value of 1.5, 10% of the sources have $Q > 2.4$ and the largest value is 5.3. The distribution appears to be independent of redshift, radio luminosity, lobe flux density ratio or whether the source is identified with a quasar or a galaxy (McCarthy et al. 1991). We can therefore use the relative symmetry of highly luminous radio sources about their optical counterparts as input to our identification procedure.

6.2. *Identification procedure: The likelihood method*

To quantify our identification procedure properly, we use a modified version of the likelihood technique which has often been used (e.g. Richter 1975; de Ruiter et al. 1977; Condon et al. 1975; Windhorst et al. 1984; Oort 1987). To assess the reliability of a proposed identification, we use as ingredients i) the observed differences between the optical and "the" radio positions, ii) the background optical counts and iii) the distribution of Q values. For the 7 sources that have an obvious radio core, we use the position of the core as the radio position. For the other sources we define the radio position as the mean of the positions of the peak intensities of the two radio lobes. Because of the known strong correlation between radio morphology and luminosity the 7 radio sources with diffuse radio morphology are not expected to be at large distances. We reject these for studying the identification statistics of the powerful sources.

We shall assume that the distribution of Q values for our USS sample is the same as for the 3C sample. This assumption appears reasonable, because the Q distribution appears not to depend strongly on relevant observables (McCarthy et al. 1991). However, we should be aware that any dependence of the Q distribution on spectral index might slightly change the resultant identification statistics.

The dimensionless position error r is defined by:

$$r = \left(\frac{\Delta\alpha^2}{\sigma_\alpha^2} + \frac{\Delta\delta^2}{\sigma_\delta^2} \right)^{\frac{1}{2}}, \qquad (1)$$

where $\Delta\alpha$ and $\Delta\delta$ are the measured position differences in right ascension α and declination δ between the position of the radio source and the optical objects, and $\sigma_\alpha^2 = \sigma_{\alpha_{\rm rad}}^2 + \sigma_{\alpha_{\rm opt}}^2$ and $\sigma_\delta^2 = \sigma_{\delta_{\rm rad}}^2 + \sigma_{\delta_{\rm opt}}^2$ are the standard deviations in the position differences.

The positional errors in our 20 cm VLA A array snapshot radio maps ($\lesssim 0.3''$) are small compared to the optical position errors ($\sim 0.9''$). For sources that do not show an obvious radio core component, the extent of the radio source, however, introduces an additional error in the standard deviations in the position of the optical identification.

We parameterise this additional uncertainty using the radio size R and the radio lobe distance ratio Q. The displacement of the central optical position in the direction of the main radio axis is given by:

$$\sigma_Q = R \left(\frac{Q-1}{2Q+2} \right). \qquad (2)$$

Since 66% ($= 1\sigma$) of the sources from the 3C sample have $Q < 1.5$ we will use Q=1.5 in our analysis. A radio source of size equal to the mean value of our imaged sample ($14''$) and with $Q = 1.5$ will have its optical counterpart displaced with $1.4''$ along the radio axis with respect to the nominal radio position.

Using σ_Q we rewrite the dimensionless variable r:

$$r = \left(\frac{\Delta\alpha^2}{\sigma_{\alpha_{\rm opt}}^2 + \sigma_{\alpha,Q}^2} + \frac{\Delta\delta^2}{\sigma_{\delta_{\rm opt}}^2 + \sigma_{\delta,Q}^2} \right)^{\frac{1}{2}}, \qquad (3)$$

where $\sigma_{\alpha,Q}^2$ and $\sigma_{\delta,Q}^2$ are the respective values of σ_Q in the right ascension and declination direction.

In estimating the reliability of each candidate identification, we will apply the likelihood method as described by de Ruiter et al. (1977), using the above definition of r. Two probabilities are defined: i) $dp(r|id)$ is the probability that a correct identification has a measured radio-optical position difference between r and $r + dr$ and ii) $dp(r|c)$ is the probability that an incorrect identification (e.g. a serendipitous source) has a value of r between r and $r+dr$.

We assume that there is no strong clustering of objects around the radio source, so that the background counts have a Poissonian distribution. Furthermore, we assume that the normalised position difference r follows a

Rayleigh distribution. The introduction of σ_Q might lead to a slight deviation from this Rayleigh distribution. We will however disregard this possible non–Rayleigh nature of σ_Q, since i) σ_Q is only a second-order correction and ii) the σ_Q distribution for 3CR sources is similar to a Rayleigh distribution. The likelihood ratio is then defined as:

$$LR(r) = \frac{\mathrm{d}p(r|id)}{\mathrm{d}p(r|c)} = \frac{1}{2\lambda} \exp\left\{\frac{r^2}{2}(2\lambda - 1)\right\}, \qquad (4)$$

with $\lambda = \pi\sigma_\alpha\sigma_\delta\rho_{\rm bg}$ where $\rho_{\rm bg}$ the background density of objects and $\sigma_\alpha^2 = \sigma_{\alpha_{\rm opt}}^2 + \sigma_{\alpha,Q}^2$ and $\sigma_\delta^2 = \sigma_{\delta_{\rm opt}}^2 + \sigma_{\delta,Q}^2$ indicate the expected position differences.

A candidate identification with a normalised position difference r is accepted as an identification if $LR(r)$ is larger than a specified cutoff value L. Since a particular choice of L also determines the reliability and completeness of the identifications, we shall postpone our choice of L until after we have discussed the reliability and completeness of the identification statistics.

In Appendix A we list the likelihood value for each candidate identification of each radio source. Sources that did no have a candidate detection in an area of $5'' \times 5''$ between the two source extremities were considered not to be detected.

6.3. *Reliability and completeness*

From the likelihood values for the sources in the sample an estimate can be made of the reliability and completeness of the identifications.

We define the identification fraction θ as the fraction of radio sources in the sample that have a correct identification.

The quantities $p(id|r)$ and $p(c|r)$ are the a posteriori probabilities that, given the fact that we have found an object at a radius r from the radio source position, it is respectively an optical identification or a confusing object. Using Bayes' theorem we relate the identification fraction θ to these two a posteriori probabilities.

$$p(id|r) = \frac{\theta LR(r)}{\theta LR(r) + 1 - \theta}, \qquad p(c|r) = \frac{1}{\theta LR(r) + 1 - \theta}. \qquad (5)$$

The completeness C of the identifications is the fraction of the number of accepted optical identifications over the number of correct optical counterparts. It is given by:

$$C = 1 - \left(\sum_{LR(r_i)<L} p(id|r_i)\right) / N_{id}, \qquad (6)$$

where N_{id} is the number of identifications and r_i is the dimensionless position error for each source (e.g. Eq. (3)).

The reliability R of the sample is the fraction of identified sources that is expected to have a correct identification. It is given by:

$$R = 1 - \left(\sum_{LR(r_i)\geq L} p(c|r_i)\right) / N_{id} \qquad (7)$$

We shall now proceed to determine the completeness and reliability of the identifications using the procedure as described above.

As initial estimation of the identification fraction θ for our sample we use the fraction of radio sources with an FRII morphology that have a candidate identification within $5'' \times 5''$ from the mean radio position. This fraction is 86% (69 out of 80 sources) Both the completeness and reliability can now be determined as function of the likelihood ratio cutoff. In Fig. 2 we give the reliability and completeness for a range of likelihood cutoffs. A spline is fitted to the data points. In the range of likelihood cutoffs from 0 to 3 the reliability only varies from 0.94 to 0.98 while the completeness varies from 1 to 0.7. We will follow de Ruiter et al. (1977) and use a likelihood ratio cutoff of 1.8. With this likelihood cutoff and initial identification fraction, we find that the completeness and reliability of the identifications are 82% and 97%. The second estimate for the identification fraction can now be found from:

$$\theta = \frac{1}{C}\left[N(LR > L) - (1 - R)N_{\rm tot}\right] / N_{\rm tot}, \qquad (8)$$

We calculate $\theta = 75\%$. With this θ, we can again calculate the completeness and reliability, and iterate until we have found a solution for θ. After two iterations, θ does not change and is found to be 70%. With this identification fraction the completeness and reliability are respectively 88% and 95%. i.e. with 80 radio sources we expect 56 good identifications. Indeed we find 53 candidates with $LR > 1.8$, of which 4 are background objects, giving a total of 49 good identifications with $LR > 1.8$, which represents 49 / 0.88 = 56 good ids.

However, candidate identifications to radio sources with a likelihood ratios less than 1.8 can still be correct identifications. e.g. 3 of the 8 sources with $0.5 < LR < 1.8$ have a measured redshift, showing that in these cases the candidate identifications were correct.

7. Parameters of the optical counterparts

After the detection and identification of the optical counterparts, their position angles, ellipticities and magnitudes were determined. These are presented in Appendix A. The magnitude adopted are "total" magnitudes, derived for each object by integrating the intensities within an area that has twice the area enclosed by the 2.5σ isophote of the object brightness (see FOCAS Manual, Valdes 1982). This procedure should include at least 90% of the total

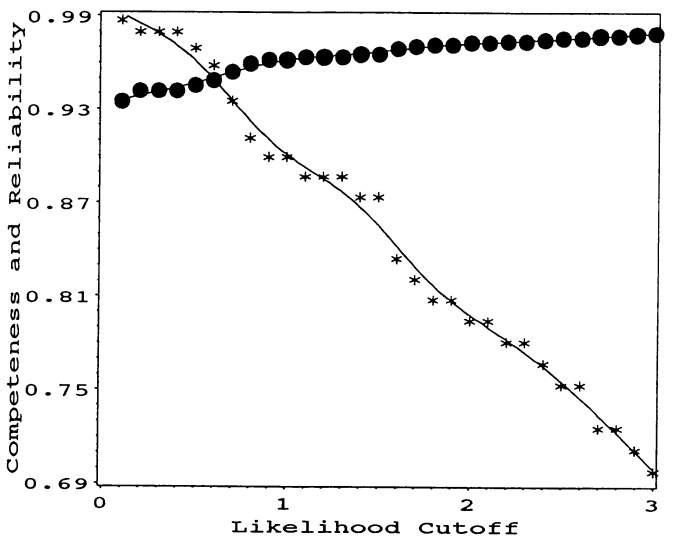

Fig. 2. The reliability (•) and completeness (∗) as a function of likelihood cutoff L (see text)

flux for typical galaxies (Kron 1980). The total magnitude for candidate identifications is listed in Appendix A.

A crude measurement of the shape of the object is its eccentricity and position angle. They can be expressed in terms of the moments of the brightness distribution (e.g. Rhee 1989). The moments were derived in the CCD coordinate system (x, y). The normalised intensity weighted moments are defined as:

$$\mu_{ab} = \frac{\sum (x - x_o)^a (y - y_o)^b I(x,y)}{\sum I(x,y)}, \qquad (9)$$

where μ_{ab} is the $a^{\rm th}$ moment in x and $b^{\rm th}$ moment in y, $I(x,y)$ is the intensity in pixel (x,y), the summation is over the pixels higher than the detection threshold and x_o, y_o is the mean (x,y) of the object (e.g. Rhee 1989). If we take $I(x,y) = 1$, we obtain the unweighted moments.

The position angle is (e.g. Hu 1962):

$$\theta = \tfrac{1}{2} \arctan \left(\frac{2\mu_{11}}{\mu_{20} - \mu_{02}} \right). \qquad (10)$$

The eccentricity e (Valdes et al. 1983) is given by:

$$e = \frac{\sqrt{(\mu_{20} - \mu_{02})^2 + 4\mu_{11}^2}}{\mu_{20} + \mu_{02}}. \qquad (11)$$

The ellipticity is:

$$\epsilon = 1 - \sqrt{\frac{1-e}{1+e}}. \qquad (12)$$

To examine how robust the determination of the position angle angle was, we have calculated the position angle from the weighted and unweighted moments μ_{ab} as described above. The differences in the determination of the position angle from a weighted and an unweighted moments is $\lesssim 12$ deg (e.g. Fig. 3). The two objects with differences > 30 deg have either a low signal to noise (e.g. 0245+013) or have a position angle in the inner regions that differs from the value in the more outer region of the object (e.g. 0946−182).

We also measured the position angle of the outer contours from the contour plots of the objects. The differences in position angle between this method and the position angle as obtained from the weighted moments are shown in Fig. 3. The differences are in general $\lesssim 30$ deg, but in 7 cases they are larger than 40 deg. The reasons for these discrepancies are mainly insufficient signal-to-noise in the outer regions of the objects to allow a a good determination of the position angle. An object with an R-magnitude of ~ 23 has a total signal-to-noise ratio of only ~ 10. The position angle as determined from the outer contours is less sensitive to a few pixels that deviate due to residual fringing, cosmic ray events and pixel to pixel variations, than the position angle as determined from the moment analysis. In what follows we therefore will use the position angle as determined from the outer contours. This is the position angle that is listed in Appendix A. For these sources we also list the ellipticity as determined from the weighted moments.

The extent of the object was measured from the extent of the outer contours (e.g. Appendix A). This measurement is not very reliable since it heavily depends on i) signal to noise in the measurement, ii) the (unknown) intrinsic brightness distribution and iii) the seeing.

8. Results

In this section we shall first present the source list. Then we shall give the magnitude and ellipticity distributions for the sources.

8.1. *Source list and maps*

The list of sources for which we have obtained CCD imaging is presented in Appendix A. For 95 objects a contour representation of an area of $45'' \times 45''$ around the radio source overlayed with a greyscale presentation of the radio source is presented in Appendix B. Contour representations of the maps of the radio sources can be found in Röttgering et al. (1994). The maps of the sources 0424+027, 1417+144 and 2231+015 are contaminated by large scale gradient on the CCD and are not shown. The map of another source (0927+064) was contaminated due to a pointing problem and is also not shown. To reduce the effect of digitisation of the contour plots, the data was spatially smoothed over 3×3 pixels using a uniform median "boxcar" function.

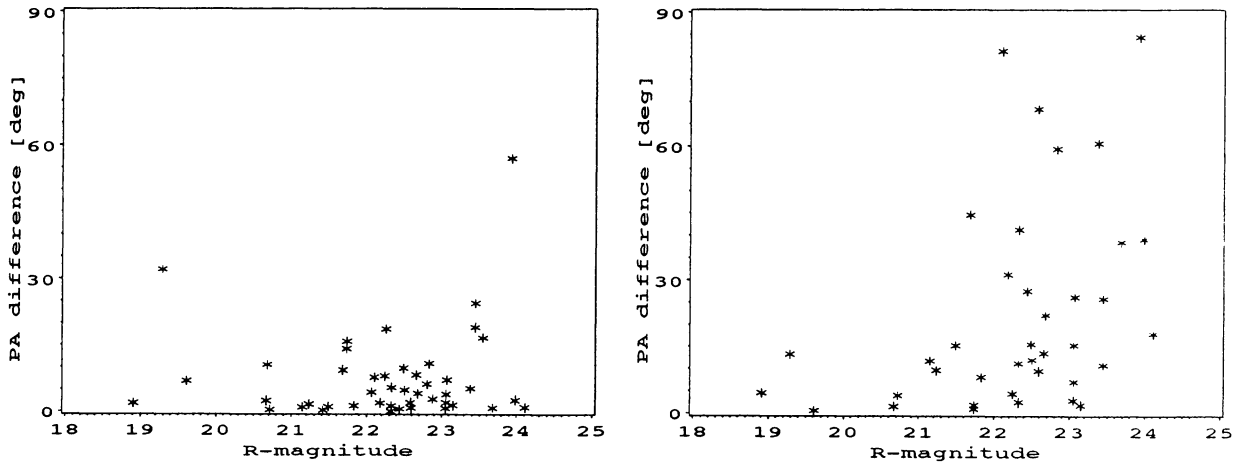

Fig. 3. The differences in various methods for measuring a position angle for the identified optical objects. Left, the differences between the position angles determined from the weighted and an unweighted moment analysis. Right, the differences between the position angles from the weighted moment analysis and that from the estimation by eye

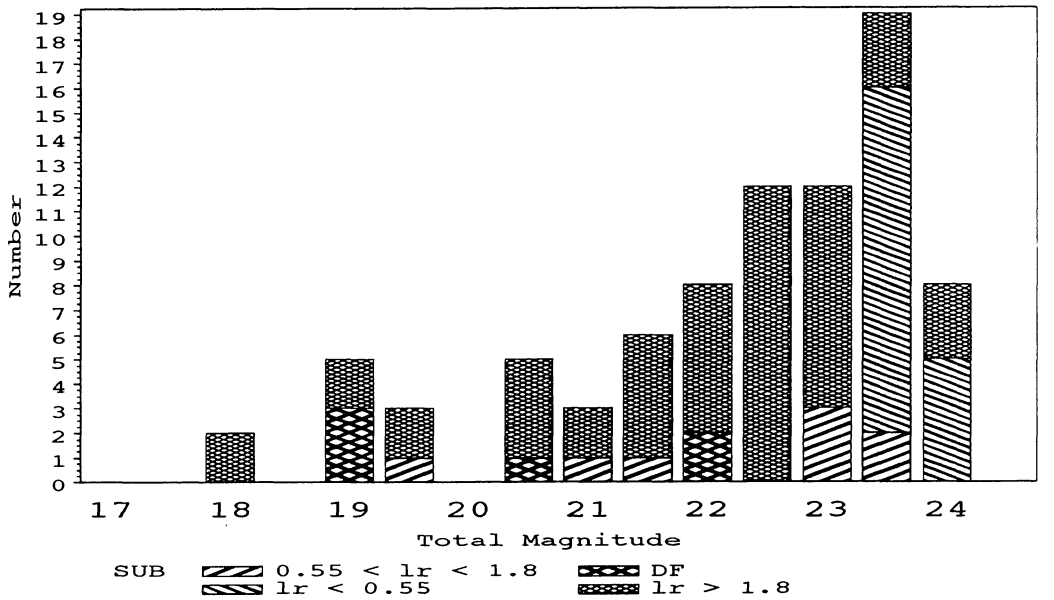

Fig. 4. R-magnitude distribution of our USS sources. Four different classes of identifications have been identified. The good identifications with $LR > 1.8$, the less reliable ones with $0.55 < LR < 1.8$, the unidentified sources with $LR < 0.55$ and the (secure) identifications with diffuse radio sources (indicated as 'DF')

8.2. *Magnitude and ellipticity distribution*

In Fig. 4 we show the magnitude distribution of the sources in the sample. Note that the distribution contains sources that have been observed when the nights were not photometric. The expected additional errors in the magnitudes of those sources are of order $\lesssim 0.5$ mag, so they should not affect the general shape of the distribution. The distribution is subdivided into the four categories.

First, the 53 sources with a good identification (e.g. $LR > 1.8$). Second, 8 sources that would be rejected as a good id on the basis of $LR > 1.8$ but have a small but non zero likelihood ratio ($LR > 0.55$) so that a significant fraction of these 8 sources are expected to be correctly identified. Third, the remaining sources (19) have likelihood ratios < 0.55 (or do not have a listed candidate with an area of $5 \times 5''$ between the two source extremities). We assessed these unidentified objects as follows. From the object counts (e.g. Fig. 1), the slope of the background galaxy count (0.37, Metcalf et al. 1991) and our adopted completeness limit of the observations ($R \sim 23$), we find that the number of sources we could have maximally missed in the 23.5 and 24 bin is 40. We

therefore distributed the 19 unidentified sources first in the bin with midpoint 23.0 in such a way that the ratio of sources in the 23.0 and 23.5 bin is consistent with the slope of the background counts. The remaining 5 sources were distributed in the bins with midpoint 24. Taking into account the incompleteness of the data for $R < 23$ (Fig. 1), the R-magnitude distribution is consistent with all the sources being associated with objects brighter then R= 24. Fourth, the sources with a diffuse radio morphology that have an obvious identification, but for which the likelihood ratio analysis is not useful are shown separately.

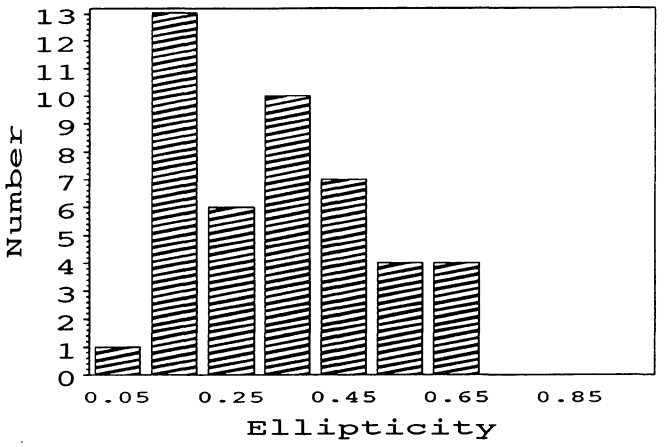

Fig. 5. The ellipticities as found from the weighted moment analysis

In Fig. 5 we show the distribution of the ellipticities for the spatially restricted counterparts of the powerful radio sources (i.e. those that are not associated with QSOs). The uncertainty in the ellipticities ranges from $\sim$ 0.1 for the brighter to $\gtrsim$ 0.25 for the fainter identification. The identified objects with the largest ellipticities (1154−041, 0028+051, 0828+193) all have multicomponent structures. It is possible that some of these components are foreground objects. The R band ellipticity distribution extends to 0.7 and has a mean of 0.33.

Rigler et al. (1992) have measured ellipticities in the B and V bands for a complete sample of 13 3C galaxies at $0.8 < z < 1.3$. Their ellipticities range from 0.1 to 0.4 with a mean of 0.19 and are less than we find for our sample. However, since our imaging data is less sensitive we do not attribute this difference to anything other than uncertainties in the measurements.

9. Conclusion

We have presented deep R band CCD imaging of 95 USS radio sources from various sub-samples of the Texas, Parkes and Molonglo catalogues. 7 of those fields were problematic, mainly due to nearby bright stars. Of the remaining 88 fields 80 contain radio sources with a non diffuse morphology. 53 of these 80 sources are identified. The reliability and completeness of the identifications were discussed using a likelihood method taking the sizes of the radio sources into account. For each identified source a total magnitude, position angle, ellipticity and and source extension was determined. The distribution of the R-magnitude peaks at $22.5 < R < 23$ and is consistent with all the sources being associated with an optical counterpart that is brighter than $R = 24$.

Acknowledgements. It is a pleasure to thank the ESO staff for their help conducting the observation. We thank Dan Golembeck for assisting us using the Guide Star Catalogue (GSC) image processing system of the Space Telescope Science Institute Hedy Versteeghe for her assistance in the project. We acknowledge the EEC for support from the Science Stimulation Programme.

Appendix A: Source list

The contents of the various columns of the table presented in this Appendix are as follows:

1. Name of the radio sample(s) to which the source belongs. The samples are described in Röttgering et al. (1994).
2. The source name in IAU B1950.0 format.
3. The position derived by fitting a quadratic function to the local intensity maxima.
4. The epoch of the coordinate system B(1950) or J(2000).
5. Total R-magnitude.
6. Optical morphological classification 'G': galaxy; 'U': unresolved (possible QSO), '-': not identified.
7. Notes: 'b': bright star hampering identification; 's' spike on the CCD frame hampering identification; 'n' no candidate identification: blank field; 'l' candidate identification rejected due to likelihood ratio too small;
8. Position angle in degrees of largest extent of the source on the maps as presented in Appendix B.
9. Ellipticity determined from the weighted moments.
10. Extension in arcseconds measured along the position angle.
11. The likelihood ratio.
12. The atmospheric conditions during the observations: '+' photometric (agreements zero points $\lesssim$ 0.1 mag, '/' nearly photometric (agreements zero points $\lesssim$ 0.5 mag).
13. Seeing in arcseconds during the observations.

Appendix A. continued

	Source	R.A.			Decl				Mag_{total}	Morph		PA	ϵ	Ext	L	Phot	Seeing
		h	m	s	°	′	″					°		″			″
(1)	(2)			(3)				(4)	(5)	(6)	(7)	(8)	(9)	(10)	(11)	(12)	(13)
365B	0008+172	0	8	32.70	17	13	9.2	B	22.6	G		145	0.5	3.5	7.4	+	0.9
365A	0008−032	0	11	11.80	−2	59	39.0	J	23.1	G		0	0.4	2.5	18.4	+	1.3
365B	0013+121							B		-	n					+	1.3
365B	0017+154							B		-	b					+	1.7
365B	0028+051	0	28	57.37	5	8	40.1	B	20.4	-	l				0.2	+	1.4
365B	0040+064	0	40	58.84	6	25	25.2	B	21.1	U					11.2	+	0.9
365B	0054+090	0	54	53.54	9	1	44.0	B	21.7	G		15	0.2	4.2	8.0	+	1.1
365B	0106+144	1	6	55.99	14	26	20.4	B	24.0	G		116	0.6	2.0	9.6	+	0.9
365B	0153+041	1	53	15.65	4	7	44.7	B	21.9	-	l				0.4	+	1.0
365A	0200+015	2	2	42.93	1	49	10.8	J	22.1	G		133	0.3	3.3	22.5	/	2.0
365B	0209+071	2	9	48.48	7	8	0.1	B	24.1	G		0	0.5	3.8	9.5	+	1.8
365A	0211−122	2	14	17.42	−11	58	46.2	J	22.7	G		98	0.1	3.0	22.4	+	1.0
365A	0224+096	2	26	44.56	9	51	37.0	J	22.2	G		93	0.4	3.1	18.9	/	2.0
365B	0226+129	2	26	11.71	12	57	13.0	B	23.4	-	l				0.0	+	1.3
408A	0230−102							J	19.5	-	b					/	2.5
365B	0245+013	2	45	12.77	1	18	53.4	B	23.9	G		30	0.0		1.9	+	1.9
365B	0251+008	2	51	7.40	0	48	32.8	B	23.0	U	l				0.9	+	0.9
365B	0310+051	3	10	47.95	5	6	3.1	B	23.1	G		129	0.3	2.9	29.1	+	1.2
365A	0325−096	3	27	51.04	−9	29	16.3	J	23.0	U	l				1.5	+	1.0
365B	0353+106	3	53	46.85	10	39	21.4	B	22.1	-	l				0.2	+	1.7
365B	0400+020							B		-	b					+	0.9
365AB	0405+125	4	5	49.64	12	32	25.8	B	22.8	U					26.3	+	1.3
365A	0417−181	4	19	43.60	−18	1	55.8	J	21.7	G	l	8	0.3	5.1	0.8	+	0.9
365A	0424+027	4	26	41.84	2	54	29.6	J		-	b				0.0	/	1.6
365B	0429+194							B		-	n					+	1.7
365A	0429−267	4	31	59.49	−26	38	10.7	J	21.5	U					10.8	+	0.8
365A	0447−164	4	50	7.47	−16	24	49.3	J	23.2	G		139	0.4	2.4	9.3	+	0.9
365B	0448+091	4	48	30.53	9	9	27.4	B	23.1	G		116	0.5	2.6	3.5	+	1.7
408A	0515−096	5	18	5.08	−9	37	2.6	J	21.6	-	s				0.2	+	1.1
365A	0545−089	5	47	29.88	−8	57	54.7	J	19.0	U					28.3	+	1.2
365B	0725+191	7	25	14.27	19	8	22.0	B	23.2	-	l				0.0	+	1.5
365B	0748+134							B		-	n					+	2.0
365B	0828+193	8	28	1.22	19	23	23.8	B	20.7	G		44	0.7	6.3	4.5	/	1.8
365B	0841+159	8	41	8.22	15	58	36.4	B	23.7	G		15	0.6		16.3	/	1.5
365B	0850+140	8	50	22.78	14	4	17.6	B	18.2	U					16.0	/	1.4
408A	0912−163	9	15	14.62	−16	30	46.6	J	21.7	G		29	0.1	2.4	25.2	+	0.9
365A	0924−134							J		-	n					+	1.0
178	0927+064							J		-	n					+	1.1
408A	0946−182	9	48	43.83	−18	28	20.2	J	19.3	G		77	0.1	6.0	4.1	+	1.0
365A	1015+187	10	17	46.54	18	32	29.8	J	21.6	-	l				0.5	+	1.1
365A	1052−163	10	55	25.72	−16	34	59.6	J	22.5	G		6	0.4	3.0	4.2	+	1.0
365A	1113−178	11	16	14.68	−18	6	23.6	J	21.4	G			0.4		11.6	+	1.0
408A	1131−269	11	33	31.45	−27	15	22.2	J	23.5	G		19	0.1	1.9	3.3	+	0.9
178	1139−025							J		-	n					+	1.0
365A	1152−245	11	54	54.12	−24	47	32.9	J	23.5	G		74	0.2	2.0	4.3	/	1.2
365A	1154−041	11	56	56.29	−4	26	30.4	J	22.1	G			0.6		7.7	/	1.4
365A	1228−166	12	30	52.87¿	−16	56	49.5	J	20.3	U					3.8	/	1.5
365A	1231−293	12	33	39.98	−29	35	7.6	J	22.1	-	l				1.8	/	1.1
178	1237−030	12	39	38.90	−3	19	2.0	J	22.4	G		14	0.5	3.5	21.1	+	1.0
365A	1238−273	12	41	27.95	−27	36	13.3	J	21.2	G		45	0.2		2.3	+	1.1

Appendix A. continued

	Source	R.A. h m s	Decl ° ′ ″		Mag_{total}	Morph		PA °	ϵ	Ext ″	L	Phot	Seeing ″
(1)	(2)	(3)		(4)	(5)	(6)	(7)	(8)	(9)	(10)	(11)	(12)	(13)
408A	1241−275	12 43 50.94	−27 52 15.0	J	18.8	G	l		0.3		0.0	+	0.9
178	1243+036	12 45 38.39	3 23 20.3	J	22.5	G	l	150	0.3	2.8	21.6	+	1.0
365A	1243−289	12 46 34.21	−29 13 53.9	J	23.6	G			0.3		1.1	+	1.9
408A	1336+003	13 38 41.21	0 2 45.0	J	22.8	G	l	34	0.1	2.0	1.4	+	
408B	1345−309			J		-	n					+	1.0
365B	1406+113			B		-	n					+	2.2
178	1410−001	14 13 15.15	−0 23 0.8	J	22.6	G		160	0.5	4.0	6.0	+	1.8
408A	1412−107	14 15 10.25	−10 57 47.6	J	22.3	G		127	0.3	2.4	29.4	+	0.9
408A	1417+144			J		-	b					/	1.1
365B	1436+157	14 36 43.14	15 44 13.0	B	19.6	G	l	131	0.4	7.0	0.8	/	1.9
365A	1452+066	14 55 9.38	6 26 54.9	J	21.2	G	l	30	0.5	3.8	0.7	/	1.1
178	1502+039	15 5 6.56	3 47 12.6	J	22.3	G		88	0.4	2.3	18.0	+	1.0
365A	1523+074			J		-	n					+	1.1
365A	1545−234	15 48 17.45	−23 37 2.0	J	22.7	G		8	0.2	2.3	26.2	+	1.0
365A	1548−111	15 51 41.84	−11 17 37.9	J	21.5	G	l	5	0.4	5.9	0.1	+	1.6
178	1558−003	16 1 17.44	−0 28 46.4	J	23.4	G	l	50	0.3	1.8	1.4	+	1.0
365B	1600+105			B		-	n					/	1.6
365B	1612+148			B		-	n					+	1.9
365B	1620+127	16 20 43.09	12 46 53.8	B	22.6	-	b				9.0	+	1.9
178	1627−013	16 30 23.87	−1 29 39.1	J		-	n				8.7	/	1.3
178	1643−031	16 45 50.68	−3 13 36.2	J	18.2	U					3.8	/	2.0
178	1657+003	17 0 16.43	0 19 22.3	J	21.3	U	l				0.5	/	1.5
365A	1718+064			J		-	bs					-	1.1
365A	1722+105	17 24 41.86	10 30 50.1	J	22.2	G		84	0.2	2.8	2.7	/	1.6
178 365A	1725+167	17 27 35.63	16 44 25.3	J	22.3	G		168	0.4	3.0	7.6	/	1.6
365A	2000−091	20 3 39.01	−9 2 39.2	J	19.3	U					6.5	+	1.2
408A	2037−085	20 40 2.01	−8 24 37.9	J	21.8	U					22.1	/	1.6
365B	2045+142	20 45 25.02	14 15 53.6	B		-	s				0.0	+	1.1
178 365B	2048+136	20 48 50.89	13 37 41.4	B	19.1	-	l				0.2	+	1.5
178	2058−041			J		-	n					/	1.4
365B	2117+120	21 17 13.75	12 3 0.3	B	18.9	G		74	0.2	7.3	6.5	+	1.2
365B	2125+152	21 25 21.39	15 14 52.5	B	21.7	U					32.3	+	1.4
178 365B	2131+162	21 31 7.66	16 15 59.7	B	20.5	-					5.4	+	1.6
178	2132−031	21 35 28.44	−2 53 50.2	J	23.2	U					3.7	/	1.3
178	2135+037			J		-	n					+	1.3
365B	2202+128	22 2 47.96	12 50 57.1	B	23.1	G		174	0.5	2.3	3.9	+	1.0
178	2205−040	22 8 7.56	−3 48 5.9	J		-	n				7.4	+	1.3
365A	2224−273	22 27 43.30	−27 5 1.6	J	22.3	U					25.1	+	1.3
365B	2226+162	22 26 17.87	16 17 53.9	B	22.3	G			0.1		12.9	+	1.1
178 365B	2231+015			B		-	b					+	0.9
408A	2236−047	22 39 32.75	−4 29 32.5	J	18.8	G		45	0.3	9.4	12.7	/	1.3
408B	2242−304	22 45 9.91	−30 12 40.8	J		-	n				15.8	+	1.0
365B	2243+174	22 43 35.25	17 28 2.3	B	20.7	G		105	0.4	6.5	3.7	+	1.4
178	2246−022	22 48 54.58	−1 59 18.1	J	22.2	-	l				0.0	/	1.8
408A	2251−089	22 53 40.40	−8 40 44.4	J	22.8	G			0.2		19.1	/	2.0
408B	2311−308	23 14 15.86	−30 37 17.4	J	20.7	G			0.1		5.2	+	1.3
365B	2317+120	23 17 36.63	12 5 40.3	B	22.9	G			0.4		7.3	+	1.1
365B	2334+178			B		-	n					+	0.9
408B	2346−320	23 48 50.60	−31 44 20.0	J	21.8	G		70	0.4	3.0	3.3	/	2.0

Appendix B: CCD images

1. 0017+154 Bright confusing star.
2. 0028+051 Of the two possible id's, the one closest to the line joining the two lobes is taken.
3. 0209+071 Two possible id's near radio source. The coordinates are for the middle clump.
4. 0226+129 Condensations between the radio lobes. The coordinates are for the clump nearest to the line connecting the two lobes.
5. 0310+051 Faint galaxy coinciding with southern lobe.
6. 0417−181 Highly elongated source. The coordinates are for the central condensation.
7. 0424+027 No contour map given.
8. 0429−267 A confusing diffraction spike of a bright star passes through the objects.
9. 0448+091 Several condensations in between the radio lobes. The coordinates are for the clump nearest to the line connecting the two lobes.
10. 0515−096 Confusing spike through galaxy. Therefore the noted magnitude is from within a 3″ aperture instead of the total magnitude as defined in the text.
11. 0924−134 Five or six candidates for the identification. Radio source in cluster?
12. 0927+064 The data was contaminated due to a pointing problem. No contour map given. Candidate identification merged with bright star. Focas splitting algorithm applied.
13. 0946−182 Strongly elongated galaxy and aligned perpendicular to the radio source.
14. 1237−030 Astrometry possibly less accurate, since it had to be done with only two galaxies.
15. 1241−275 Identification also visible on STScI GSC plates.
16. 1417+144 Bright confusing star nearby. No contour map given.
17. 1436+157 A two component object. Coordinates are for the brightest component.
18. 1545−234 Confusing diffraction spikes of bright star in the CCD field.
19. 1548−111 Clumpy galaxy with at least three lumps. Coordinates for the brightest lump.
20. 1620+127 Three objects near radio position. The coordinates are for the object that is closest to the radio source.
21. 1643−031 Two bright candidate id's in the middle of the two lobes.
22. 1657+003 At least 4 bright candidate id's between the radio lobes.
23. 1718+064 Confusion by diffraction spike from nearby star.
24. 1725+167 Bright star nearby.
25. 2000−091 A possible QSO.
26. 2048+136 For this relatively large radio source at least 5 possible id's.
27. 2205−040 Two possible id's. The coordinates are for the brightest candidate.
28. 2226+162 Two clumps of equal magnitudes The coordinates are for the clump closest to the centre of the radio source.
29. 2231+015 Strong gradient on CCD due to scattered light of bright nearby star. No contour map given.
30. 2246−022 Trail of radio emission passes two possible id's.

Appendix B. continued

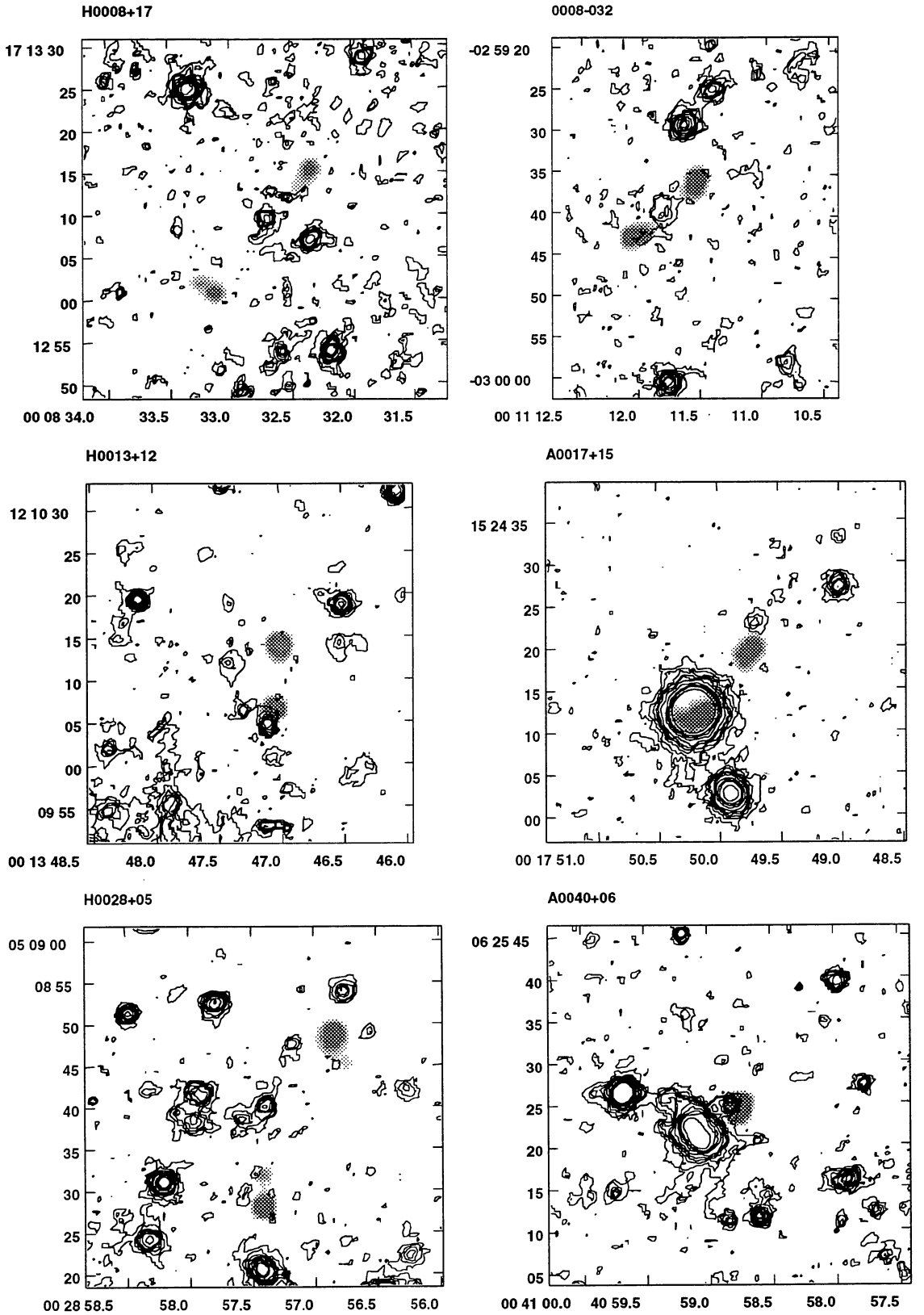

Appendix B. continued

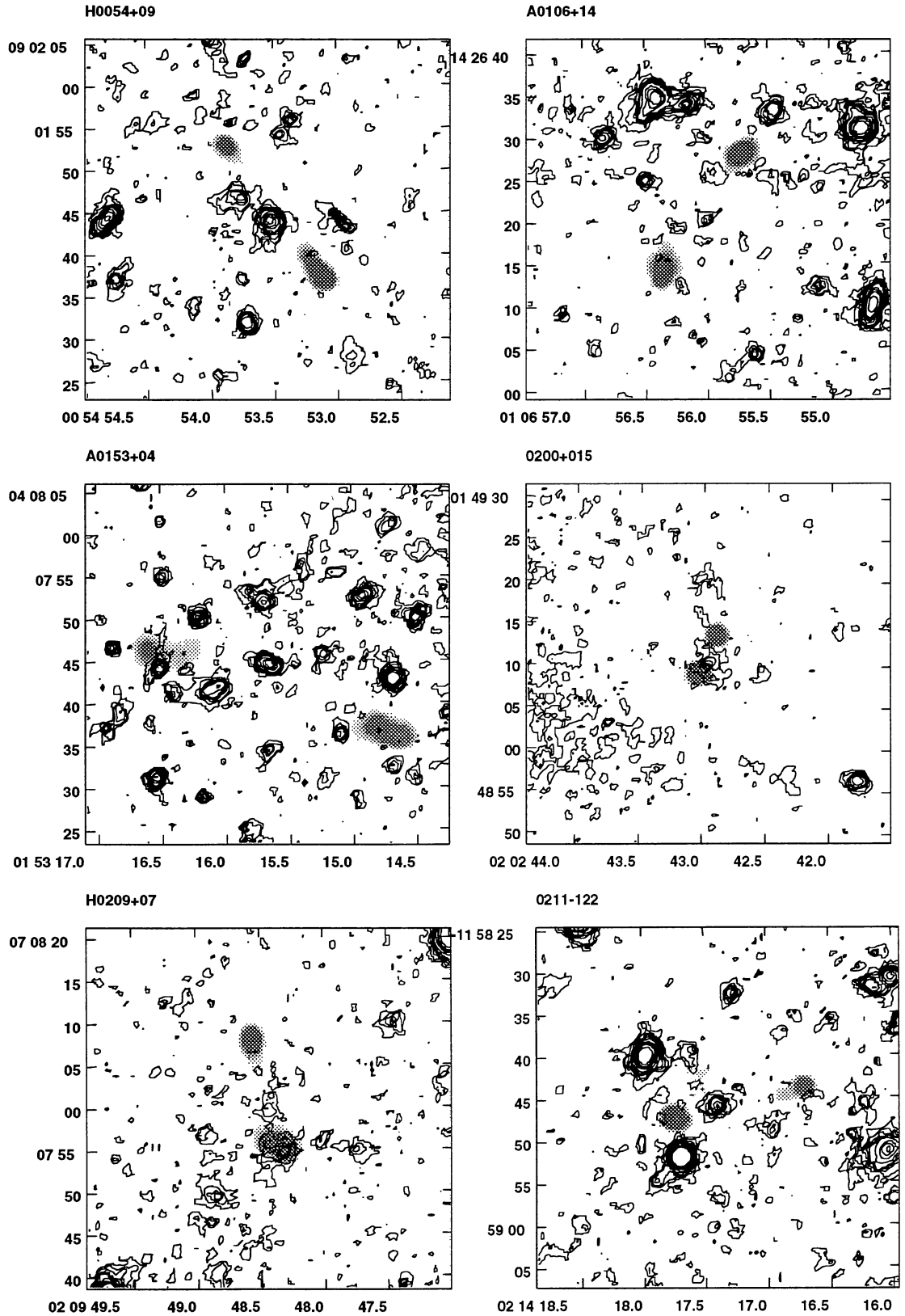

Appendix B. continued

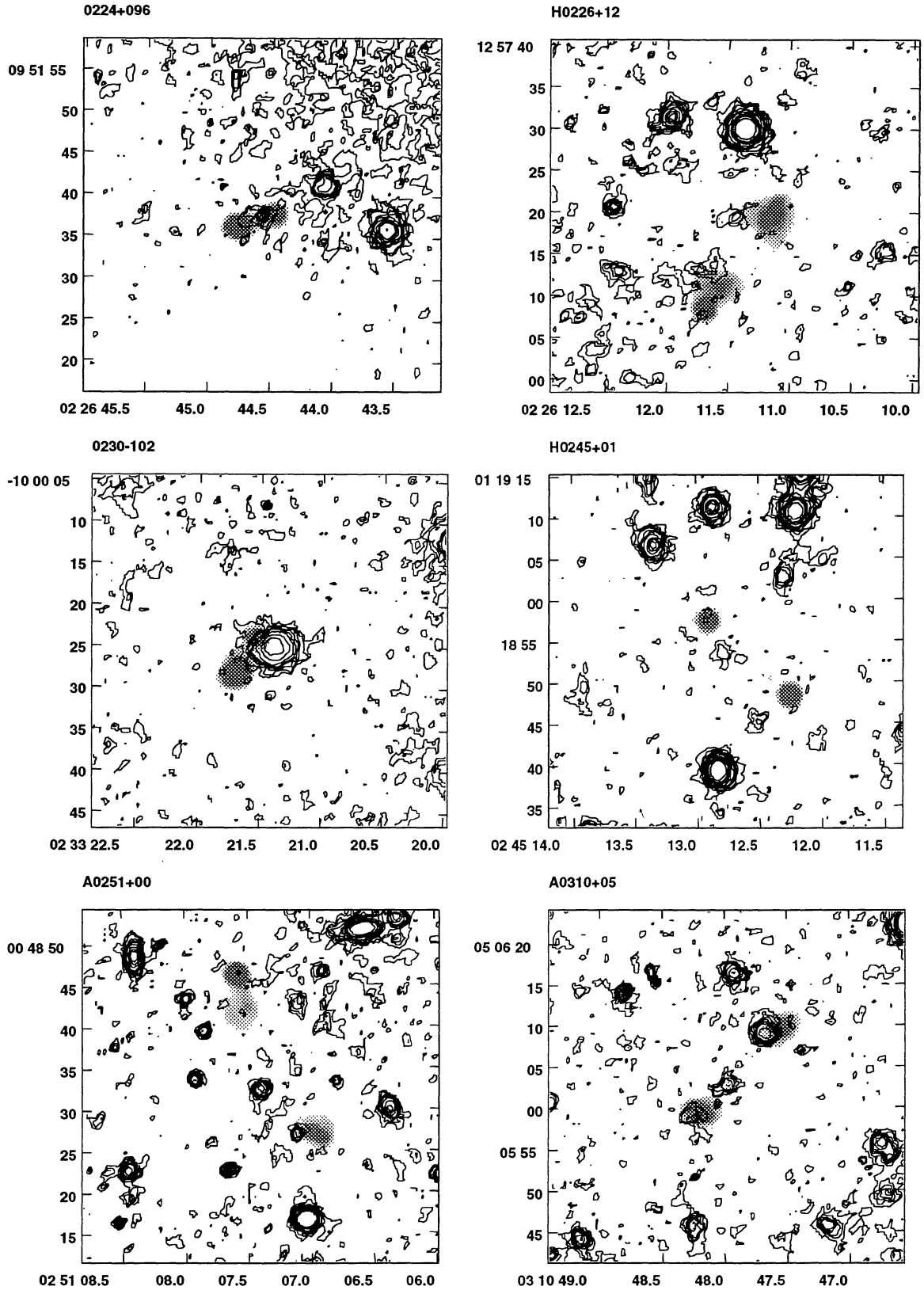

Appendix B. continued

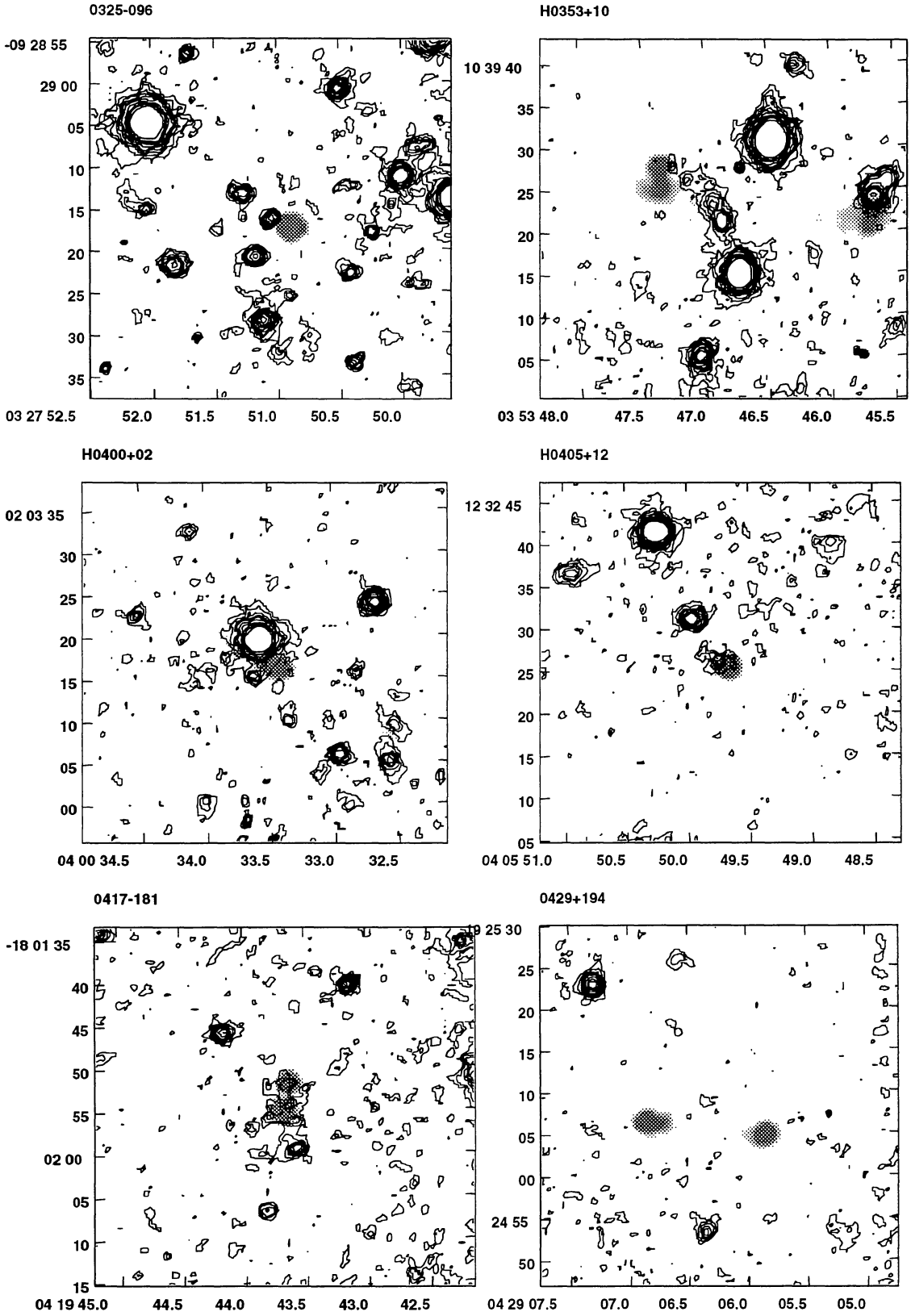

Appendix B. continued

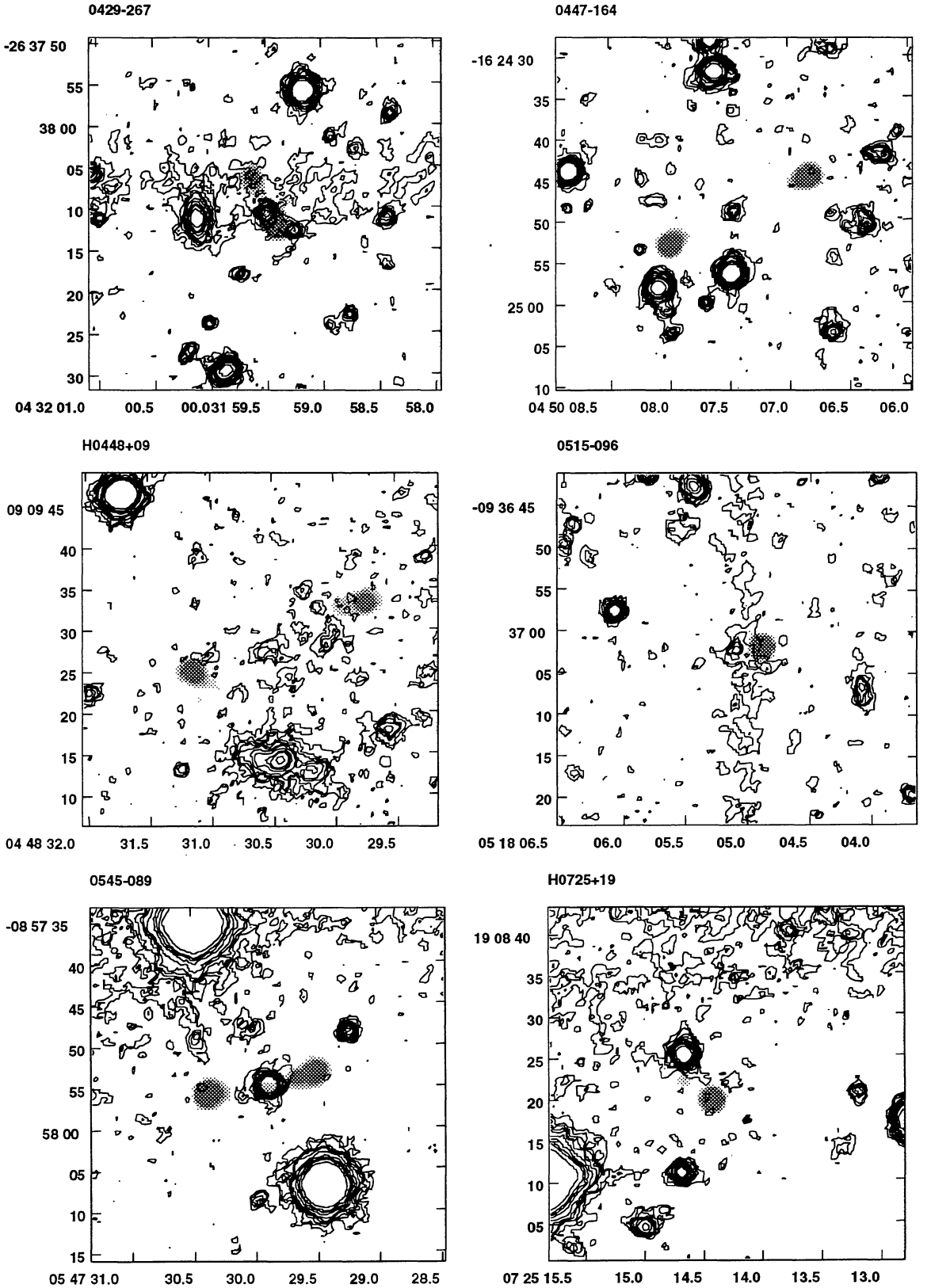

Appendix B. continued

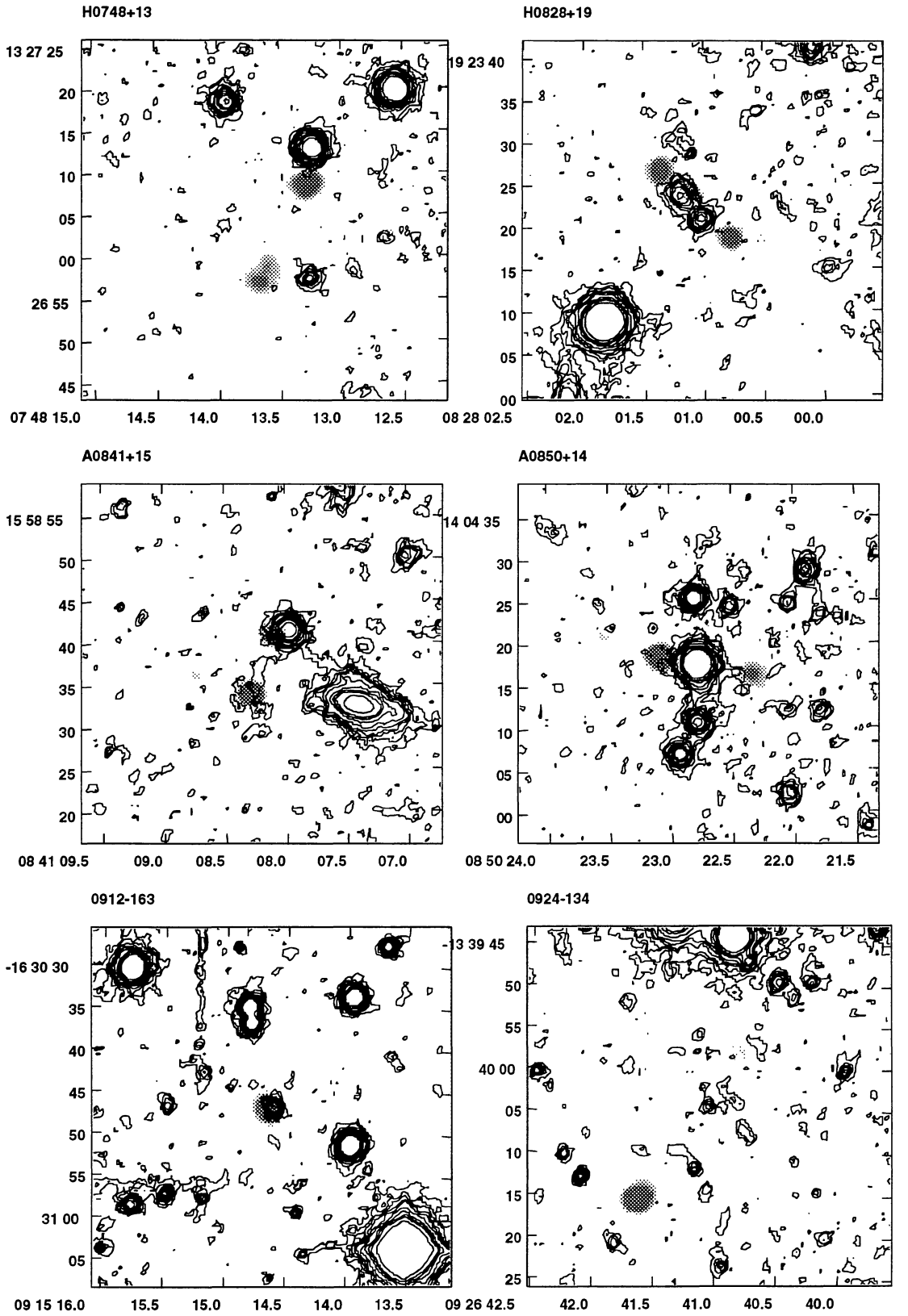

Appendix B. continued

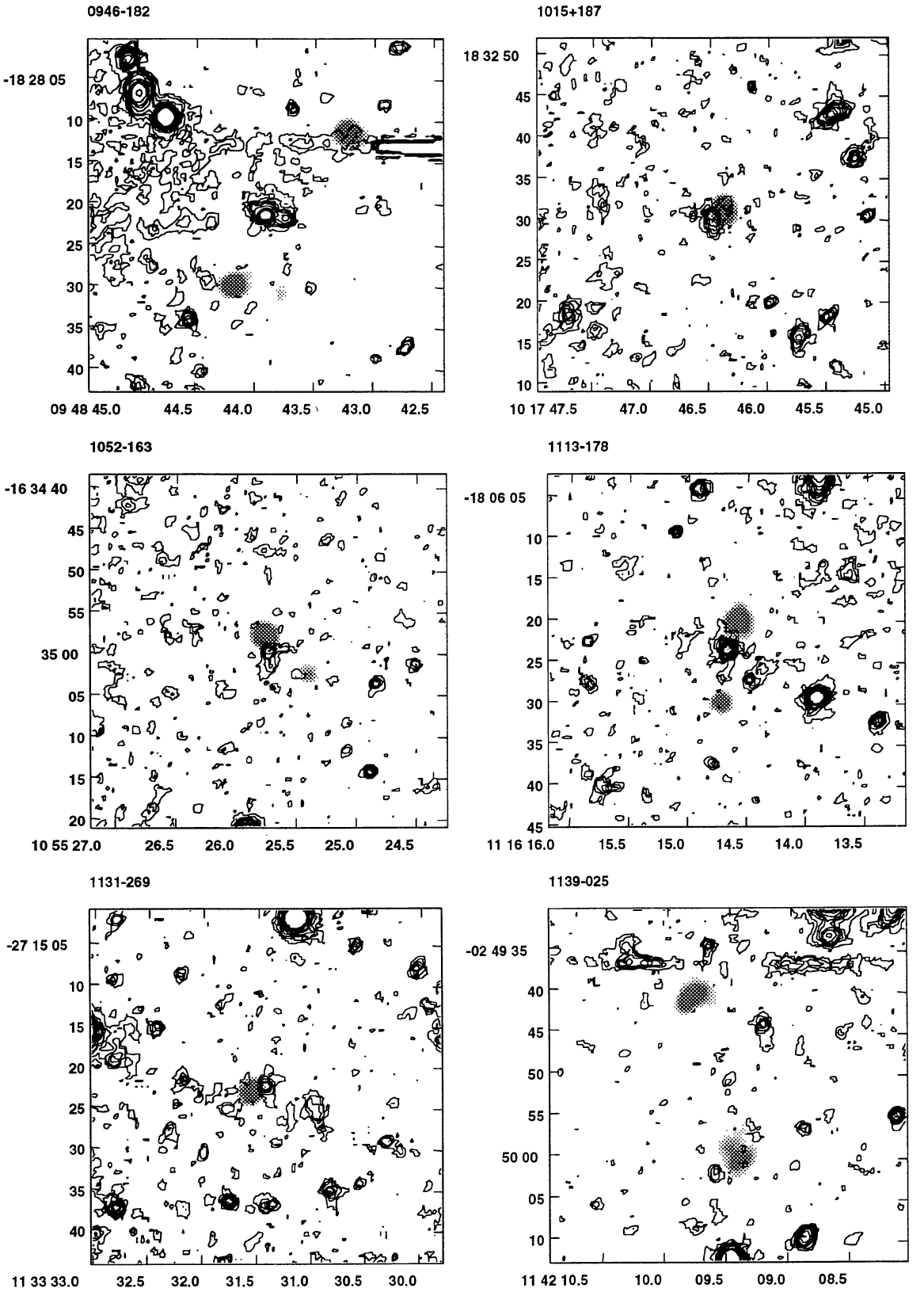

Appendix B. continued

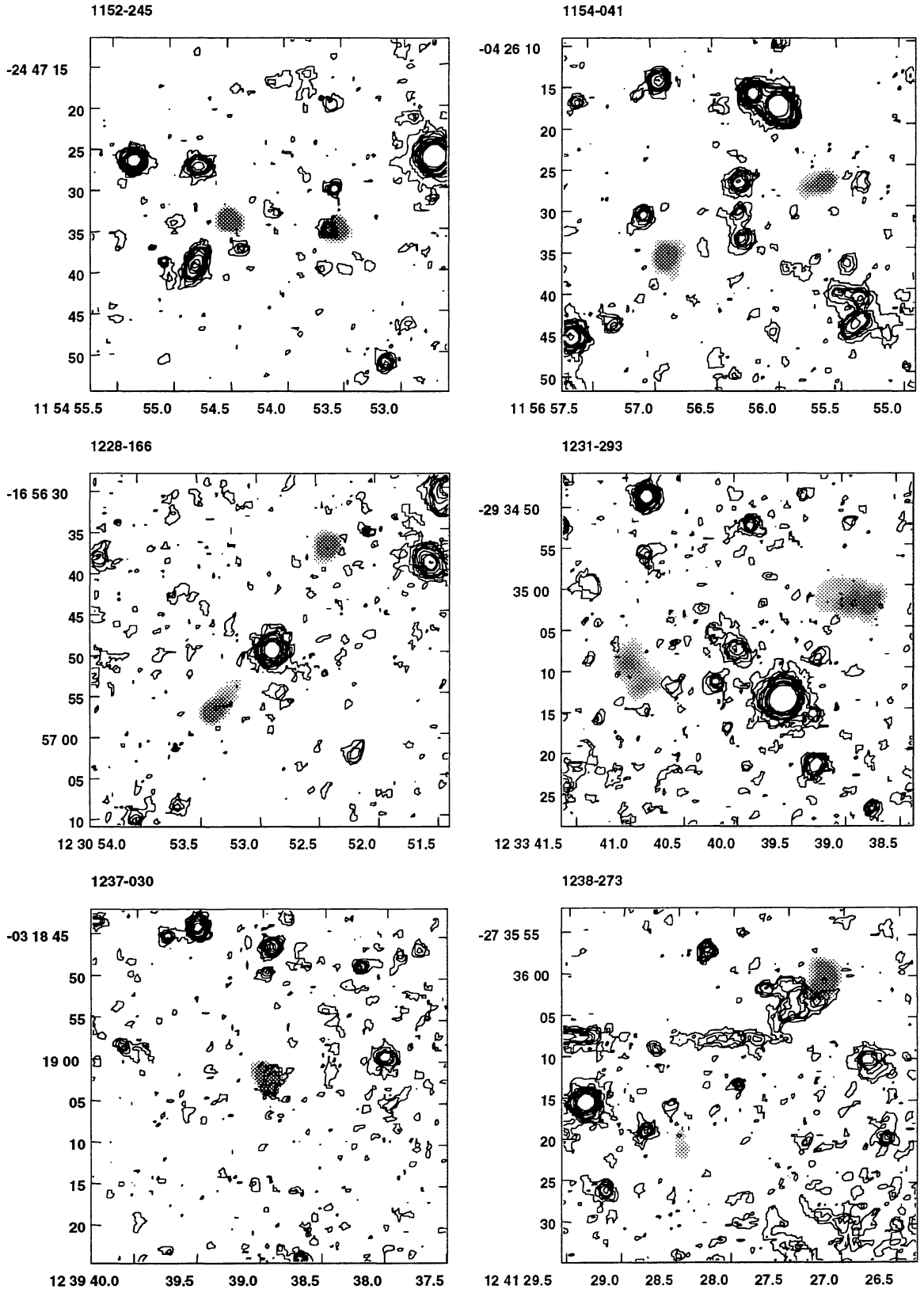

Appendix B. continued

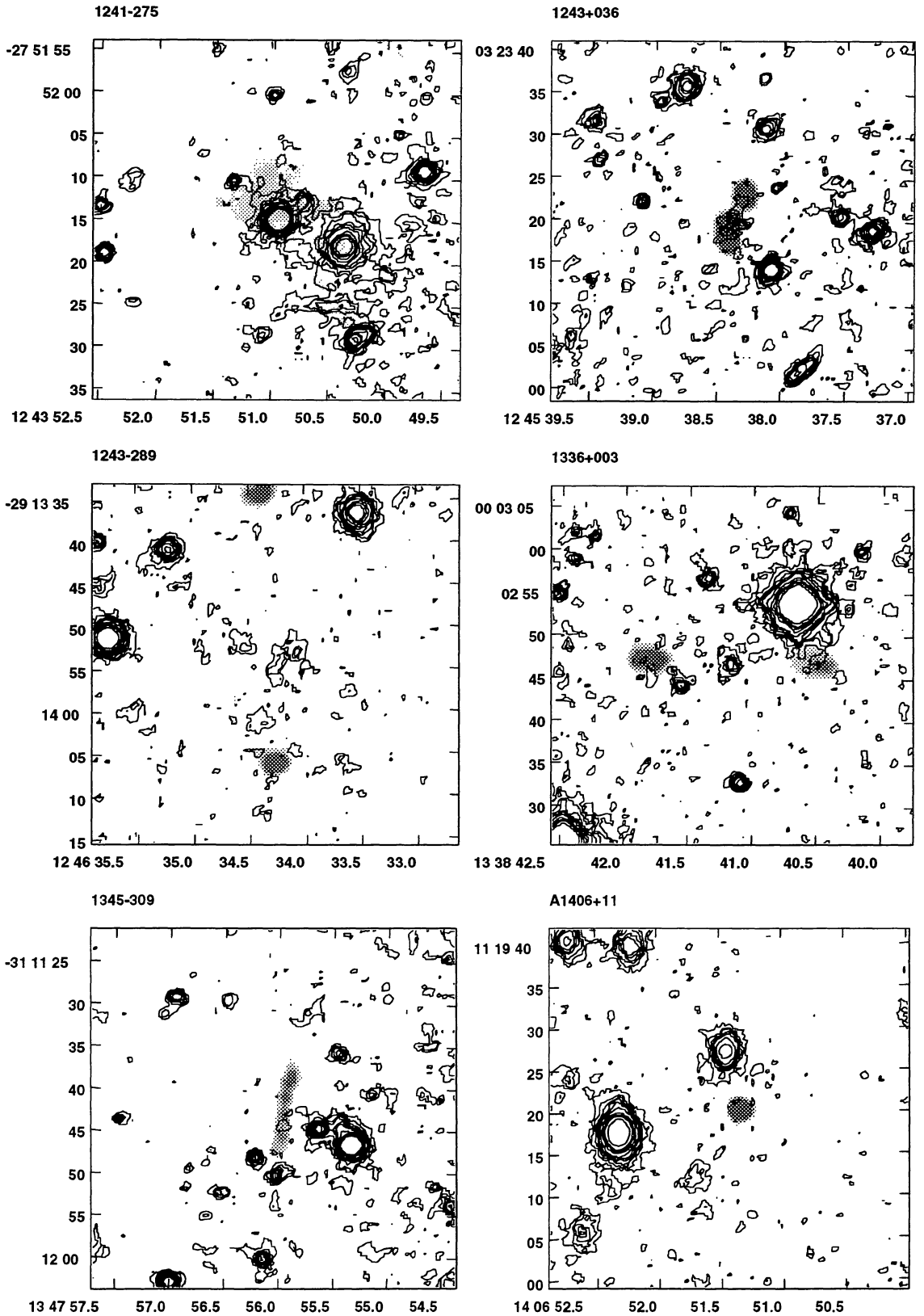

Appendix B. continued

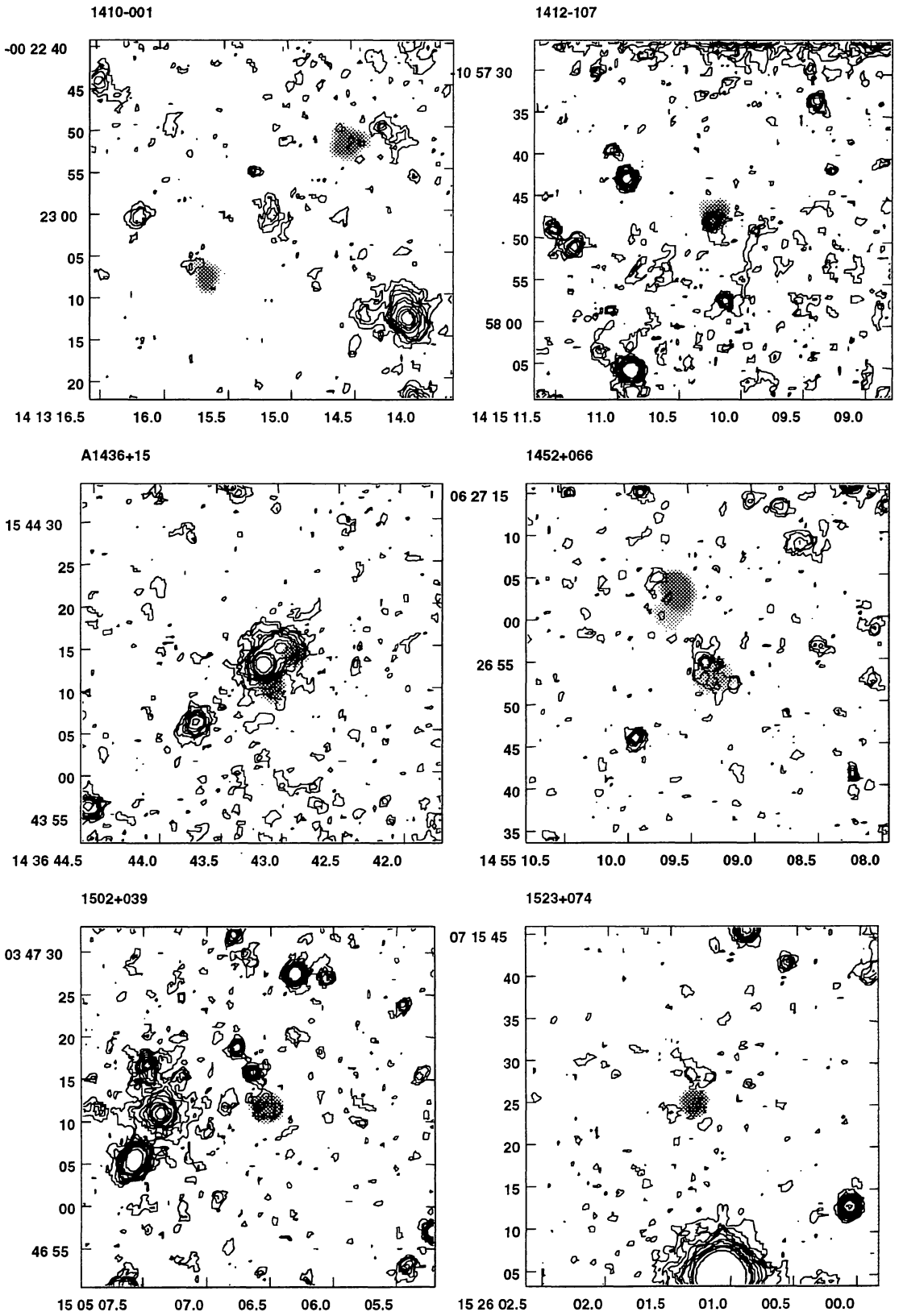

Appendix B. continued

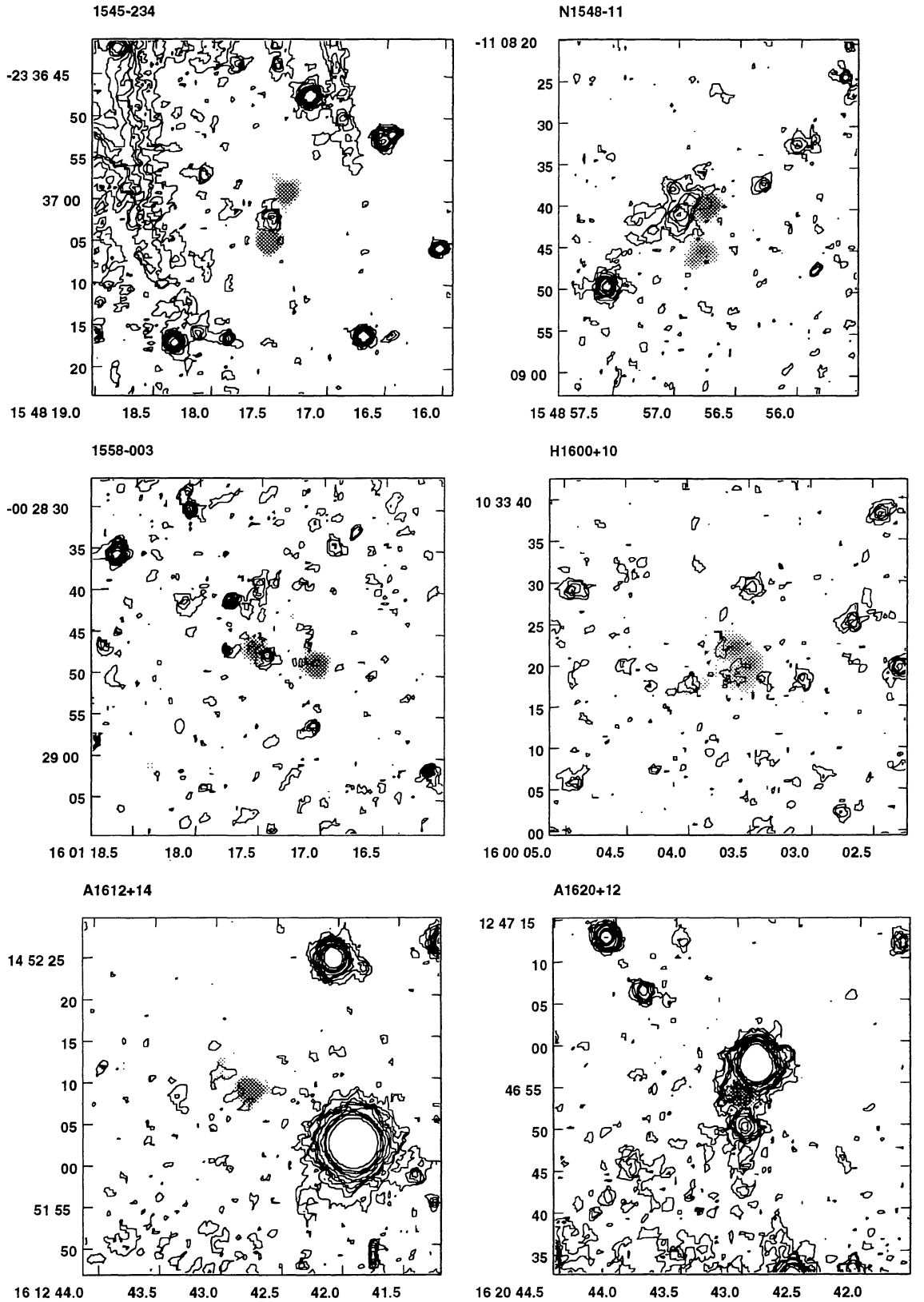

Appendix B. continued

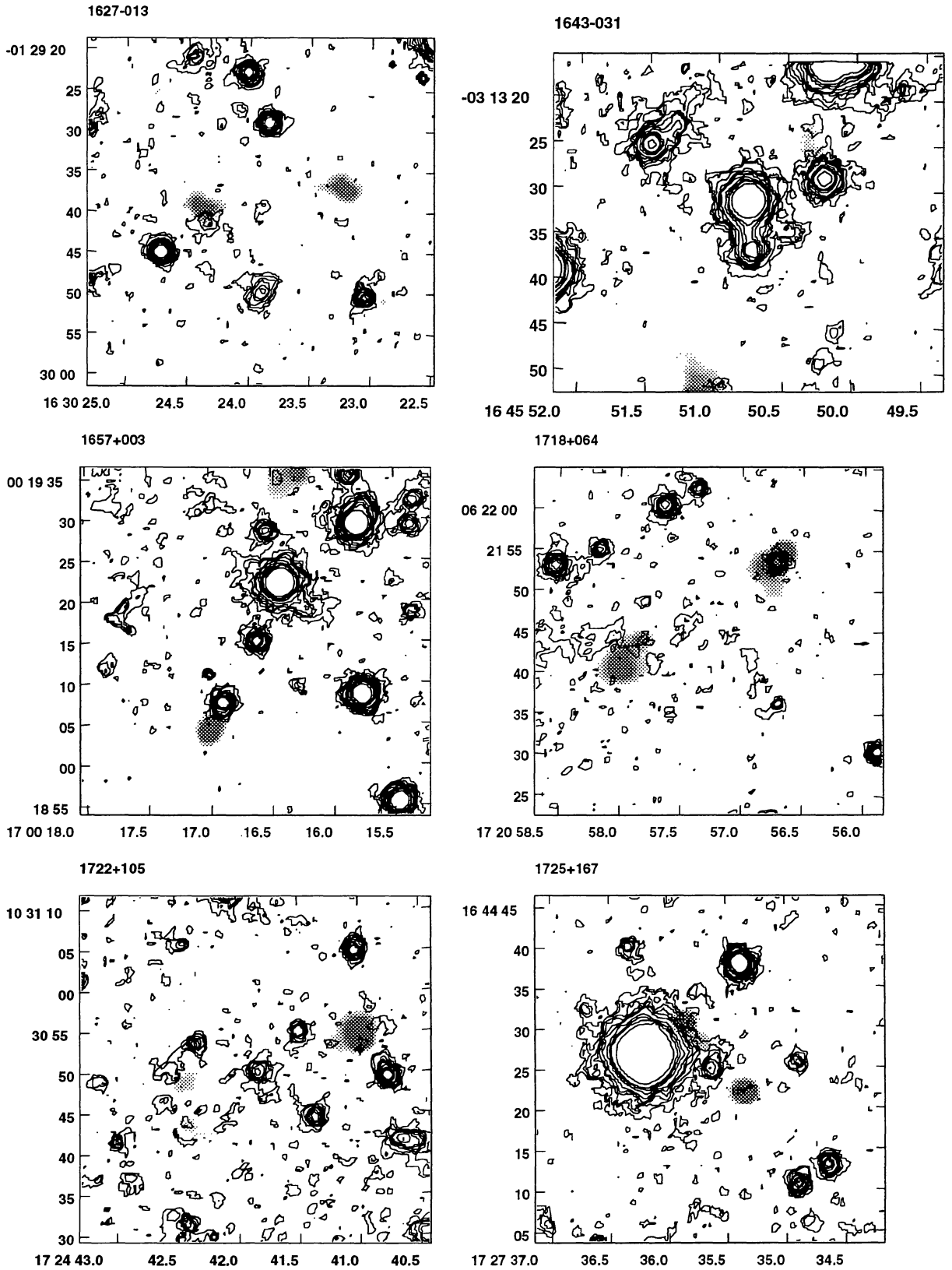

Appendix B. continued

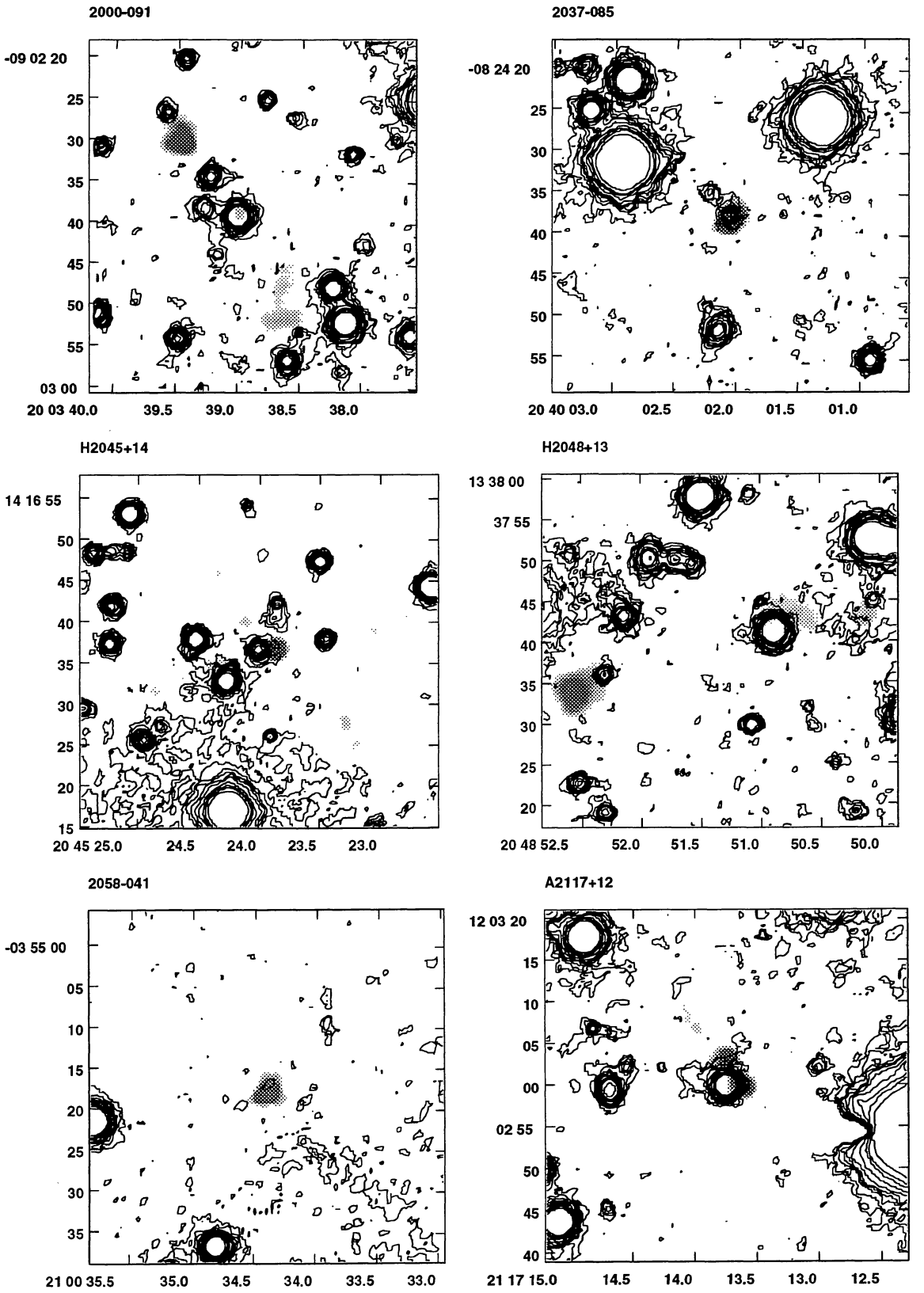

Appendix B. continued

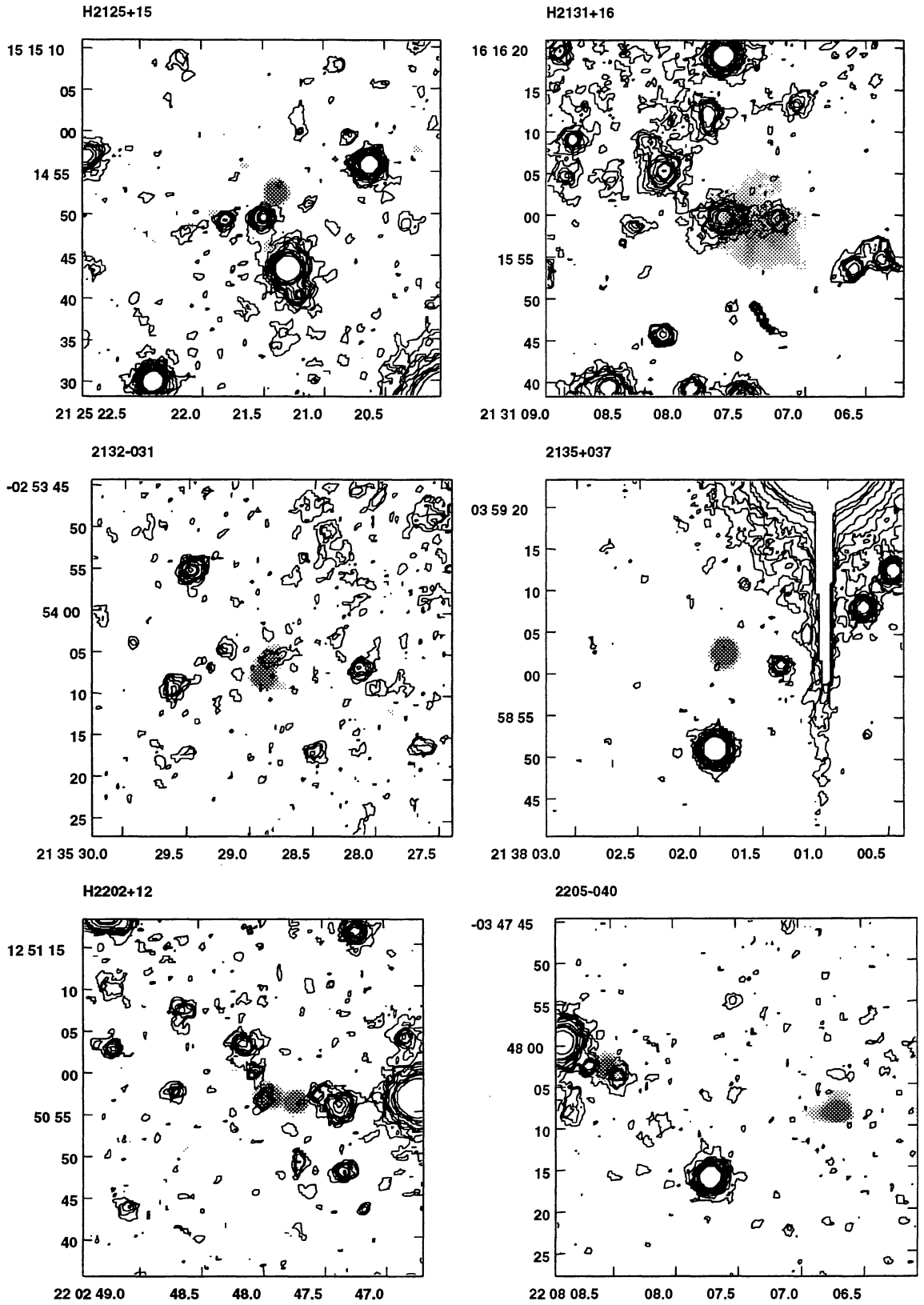

Appendix B. continued

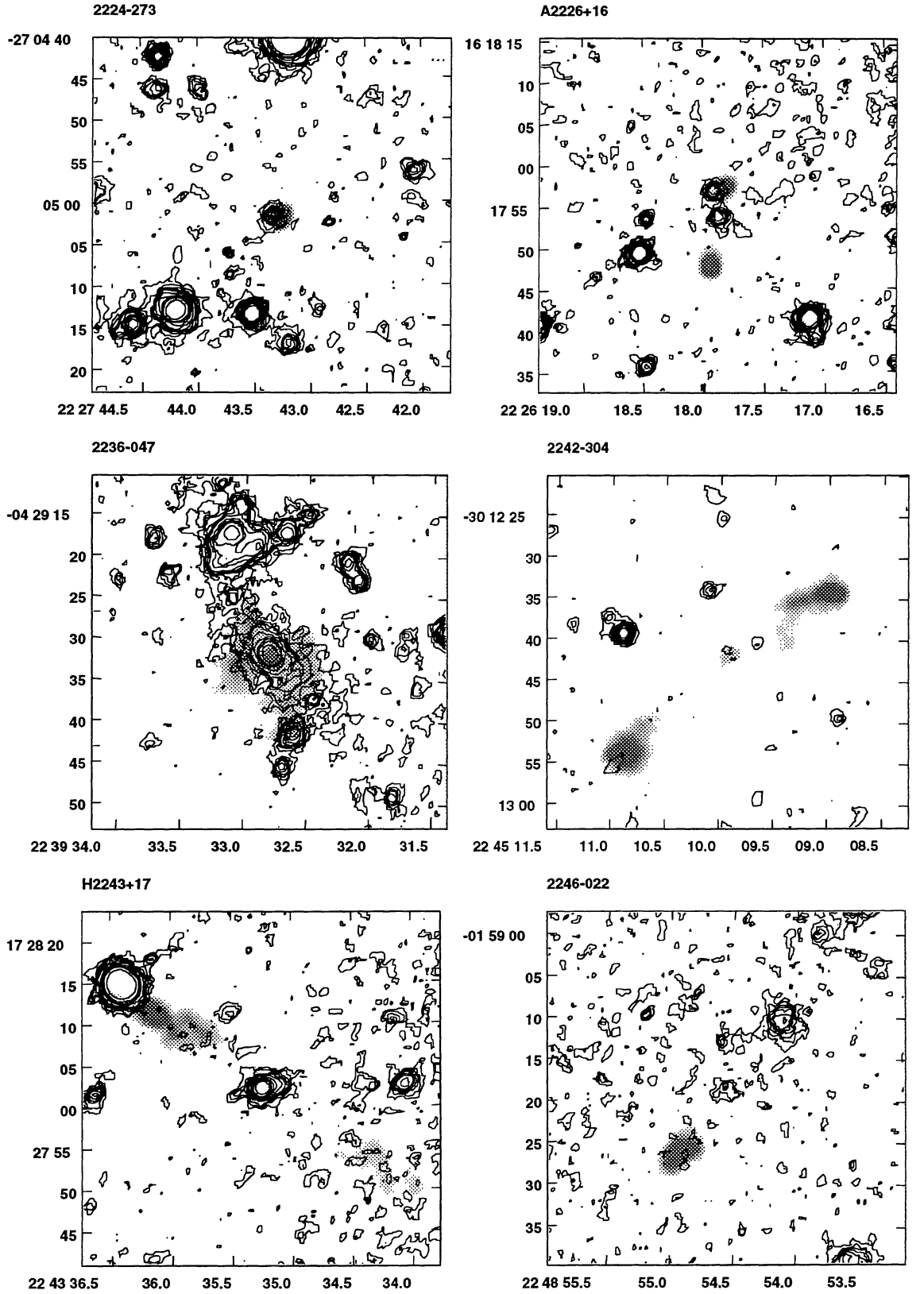

Appendix B. continued

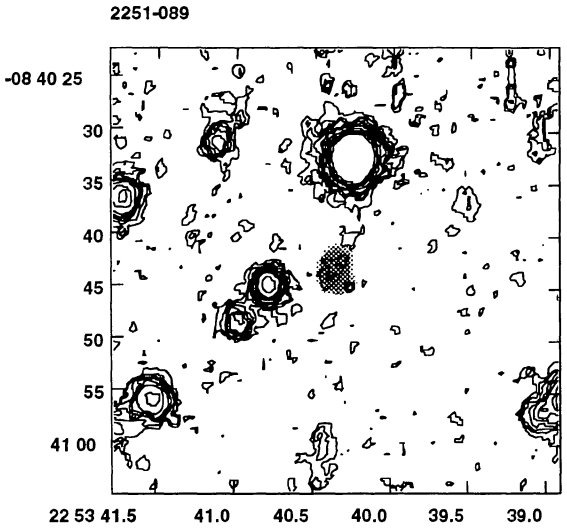

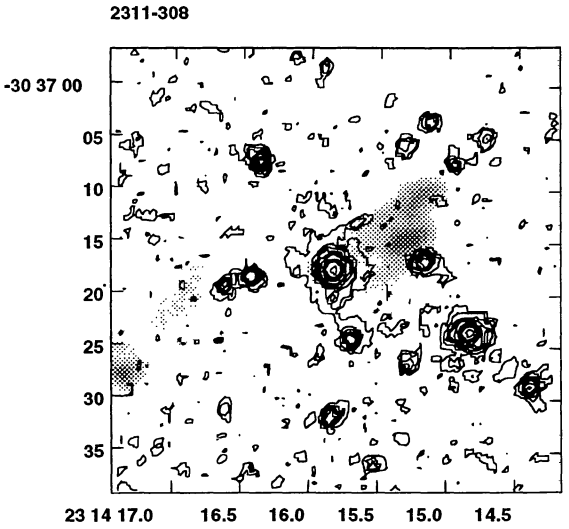

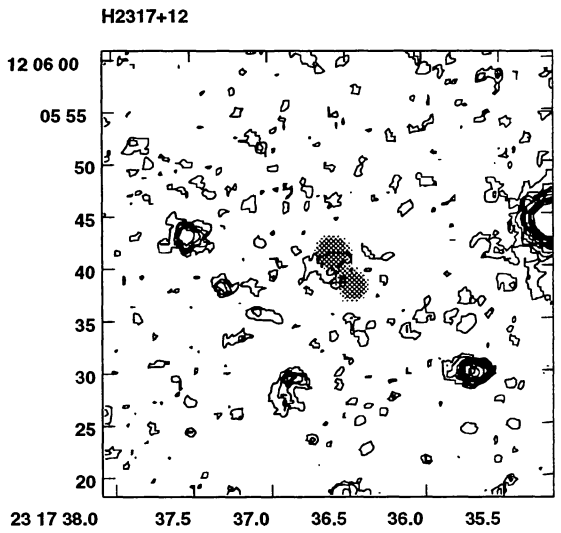

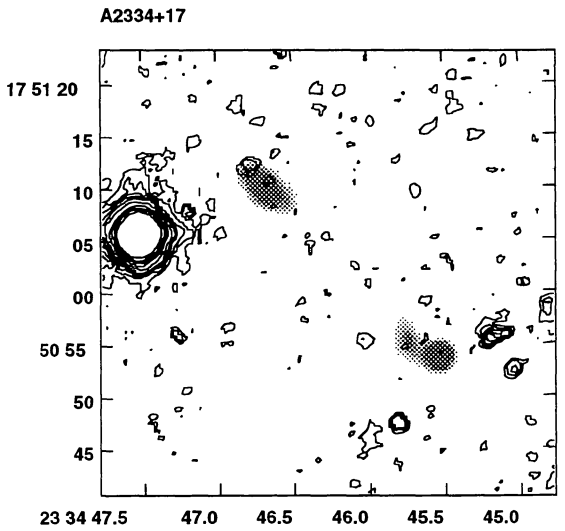

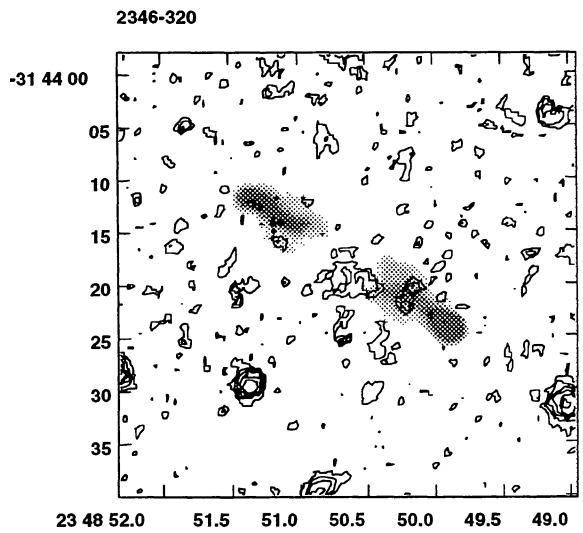

References

Bahcall J.N., Soneira R.M., 1984, ApJ 55, 67

Bennett A.S., 1962, Mem. R. Astr. Soc. 68, 163

Chambers K.C., Miley G., 1989. In: Kron R.G. (ed.); The Evolution of the Universe of galaxies: The Edwin Hubble Centennial Symposium. San Francisco: Astro. Society of the Pacific, p. 373

Condon J.J., Balonek T., Jauncey D.L., 1975, AJ 80, 887

de Ruiter H., Willis A., Arp H., 1977, A&AS 28, 211

Graham J., 1982, PASP 94, 244

Hill G., Lilly S., 1991, ApJ 367, 1

Hu Ming-Kuei, 1962, I.R.E. Trans. on information theory Feb., 179

Kron R., 1980, ApJS 43, 305

Laing R.A., Riley J.M., Longair M.S., 1983, MNRAS 204, 151

Lasker B., Sturch C.R., McLean B.J., Russel J.L., Jenker H., Shara M., 1990, AJ 99, 2019

McCarthy P.J., van Breugel W., Kapahi V.K., 1991, ApJ 371, 478

Metcalfe N., Shanks T., Fong R., Jones L., 1991, MNRAS 249, 498

Miley G., Chambers K., 1989. In: Meurs E.J.A. and Fosbury R.A.E. (eds.), ESO Workshop on Extranuclear Activity in Galaxies, p. 43

Rhee G., 1989, Ph. D. Thesis, University of Leiden

Richter G., 1975, Astron. Nachr. 296, 65

Rigler M., Lilly S., Stockton A., Hammer F., Le Fèvre O., 1992, ApJ 385, 61

Röttgering H.J.A., 1993, Ph. D. Thesis, University of Leiden

Röttgering H.J.A., Lacy M., Miley G., Chambers K., Saunders R., 1994, A&A 108, 79

Schwarz H.E., Melnick J. 1989, The ESO Users Manual

Tyson J.A., 1988, AJ 96, 1

Valdes F., 1982, Faint Object Classification and Analysis System, NOAO

Valdes F., Tyson J.A., Jarvis J.F., 1983, ApJ 271, 431

Windhorst R.A., Kron R.G., Koo D.C., 1984, A&AS 58, 39